International Journal for Numerical Methods in Engineering

WILEY

RESEARCH ARTICLE OPEN ACCESS

On the Extension of Mesh-Distortion-Insensitive Petrov-Galerkin Finite Element Formulations to Linear Elastodynamics

Felix Zähringer | Peter Betsch

Institute of Mechanics, Karlsruhe Institute of Technology (KIT), Karlsruhe, Germany

Correspondence: Peter Betsch (peter.betsch@kit.edu)

Received: 13 March 2026 | **Revised:** 14 May 2026 | **Accepted:** 5 June 2026

Keywords: elastodynamics | finite element method | mesh distortion | Petrov-Galerkin

ABSTRACT

Numerous mesh-distortion-insensitive Petrov-Galerkin finite element formulations have been developed for the simulation of elastostatic problems. This contribution presents initial results on how these formulations can be extended to linear elastodynamics. In this context, three different approaches are examined, building upon an established 8-node elastostatic formulation. The first two approaches demonstrate that preexisting strategies reach their limits when applied to such unsymmetric formulations. In contrast, the novel third approach enables stable simulations. Moreover, the resulting formulation appears to be less sensitive to mesh distortion than a standard 8-node Bubnov-Galerkin formulation.

1 | Introduction

It is well known that the quality of finite element (FE) simulations in the field of solid mechanics depends strongly, among other factors, on the mesh that is used. In particular, when using conventional displacement-based FE formulations, the element geometry has a significant influence on the quality of the solution. For example, parallelogram-shaped elements should ideally be used for the simulation of two-dimensional problems, as elements with other geometries typically lead to significantly poorer numerical results. An explanation for this phenomenon is provided, for example, in Lee and Bathe [1].

However, in many practical applications, meshes with distorted elements are unavoidable due to the geometry of the simulated structure. For this reason, efforts have been made for some time to reduce the sensitivity of finite elements to mesh distortion. In this context, a number of element formulations have been developed that can be classified as Petrov-Galerkin FE formulations. In contrast to conventional Bubnov-Galerkin FE formulations, where the test and trial functions are approximated using the same ansatz functions, Petrov-Galerkin formulations employ different ansatz functions for the approximation of the test and trial functions. In the linear elastostatic case, this special discretization technique leads to

a stiffness matrix that is, in general, unsymmetric. Consequently, such formulations are often referred to as unsymmetric FE formulations.

Fundamental to the development of these mesh-distortion-insensitive formulations is the pioneering work of Rajendran and Liew [2]. In this work, an 8-node Petrov-Galerkin FE formulation is introduced that is capable of exactly reproducing quadratic displacement fields even when meshes with highly distorted elements are used. This represents a clear improvement over conventional 8-node Bubnov-Galerkin FE formulations. These enhanced properties regarding mesh distortion sensitivity can typically also be observed in simulations of more complex problems.

A major drawback of the formulation proposed by Rajendran and Liew [2] is that it is frame-dependent. As shown in [3], different results are obtained when the same problem is simulated using different coordinate systems. A remedy for this problem is provided in Xie et al. [4], where the use of so-called skew coordinates, which were originally introduced in Yuan et al. [5], is proposed. The resulting 8-node finite element formulation *UQ8** is frame-independent and constitutes a key component of the present work.

In the last few years, many other mesh-distortion-insensitive Petrov-Galerkin FE formulations have been developed based on different approaches and for various applications. Since a comprehensive review of all publications would be beyond the scope of this work, only an overview of those formulations specifically developed for the simulation of linear elastostatic problems is given in the following. A more comprehensive literature review can be found in [6].

For the two-dimensional case, in addition to the aforementioned works [2–4], further 8-node element formulations were introduced in [7–9]. Formulations for 4-node elements are presented in [4, 10–15], and a formulation for triangular 6-node elements is covered in [16]. Quadrilateral elements with different approximation orders are examined in [6].

For the simulation of three-dimensional problems, 20-node elements were introduced in [4, 17]. Formulations for 8-node hexahedral elements can be found in [4, 13, 15, 18].

To the best of the authors' knowledge, the existing publications on mesh-distortion-insensitive Petrov-Galerkin FE formulations are limited to time-independent problems.[1] This is likely due to the fact that the extension of these formulations to time-dependent problems is not straightforward, as demonstrated in the present work for the case of linear elastodynamics.

This issue is not only limited to mesh-distortion-insensitive Petrov-Galerkin finite element formulations, but also restricts the applicability of many other methods that ultimately lead to unsymmetric system matrices. According to Wang and Hillman [20], this can be explained, in the case of linear elastodynamics, by the fact that, when unsymmetric system matrices are present, the satisfaction of the global energy balance cannot be guaranteed – a condition that must be fulfilled from a physical standpoint.

Nevertheless, it seems desirable to be able to exploit the advantageous properties of the aforementioned Petrov-Galerkin FE formulations with respect to mesh distortion sensitivity in the simulation of time-dependent problems. For this reason, the present work investigates three different approaches that aim to extend these mesh-distortion-insensitive formulations to the dynamic regime. The study focuses on the *UQ8** formulation by Xie et al. [4], whose computer implementation is straightforward. However, many of the insights gained can likely be applied to other Petrov-Galerkin FE formulations as well.

The paper is organized as follows. First, in Section 2, the key concepts of the underlying elastostatic *UQ8** formulation are summarized. Subsequently, in Section 3, three different approaches are presented that aim to extend this formulation to the dynamic regime. The first approach, covered in Section 3.1, represents the most straightforward way for this extension. It reflects the procedure that is typically used for Bubnov-Galerkin formulations. In Section 3.2, an approach proposed by Wang and Hillman [20] for other Petrov-Galerkin formulations is adapted to the *UQ8** formulation considered in this work. Finally, Section 3.3 introduces a novel approach based on the introduction of the velocity field as an independent variable. In Section 4, the properties of the aforementioned approaches are investigated numerically using several examples.

2 | A Mesh-Distortion-Insensitive 8-Node Petrov-Galerkin Finite Element Formulation for Elastostatics

In this section, the key concepts of the 8-node Petrov-Galerkin FE formulation *UQ8**, as introduced by Xie et al. [4], are summarized. This irreducible formulation is notable for its ability to accurately reproduce quadratic displacement fields even when highly distorted finite element meshes are used. As this formulation is relatively simple compared to other formulations, it is employed in Section 3 to demonstrate how the dynamic extension of Petrov-Galerkin finite element formulations can be achieved.

Following standard conventions, a two-dimensional linear-elastic continuum body Ω is considered. Employing a Cartesian coordinate system, every point within the body can be addressed by a position vector $\mathbf{x} = [x,\ y]^{\mathrm{T}} \in \Omega$. The displacement of each point of the body is described by the displacement field $\mathbf{u}(\mathbf{x}) = [u_x(\mathbf{x}),\ u_y(\mathbf{x})]^{\mathrm{T}}$. The boundary of the body, denoted by $\partial\Omega$, can be divided into a Dirichlet boundary $\partial\Omega_u$, where prescribed displacements $\bar{\mathbf{u}}$ are imposed, and a Neumann boundary $\partial\Omega_t$, where prescribed traction forces $\bar{\mathbf{t}}$ are applied. We assume that $\partial\Omega_u \cup \partial\Omega_t = \partial\Omega$ and $\partial\Omega_u \cap \partial\Omega_t = \emptyset$ hold for these boundaries.

The strain state at each point of the body can be characterized by the strain tensor

$$\boldsymbol{\varepsilon}(\mathbf{u}) = \begin{bmatrix} \varepsilon_{xx} & \varepsilon_{xy} \\ \varepsilon_{yx} & \varepsilon_{yy} \end{bmatrix} = \frac{1}{2}\left(\nabla_{\mathbf{x}}\mathbf{u} + \left(\nabla_{\mathbf{x}}\mathbf{u}\right)^{\mathrm{T}}\right), \tag{1}$$

which is symmetric, that is, $\varepsilon_{xy} = \varepsilon_{yx}$.

This allows the weak form commonly used in the simulation of elastostatic problems to be stated as

$$\int_{\Omega} \boldsymbol{\varepsilon}(\mathbf{w}_{\mathbf{u}}) : \mathbb{C} : \boldsymbol{\varepsilon}(\mathbf{u})\, \mathrm{d}A = G^{\mathrm{ext}}, \tag{2}$$

where $\mathbf{w}_{\mathbf{u}}(\mathbf{x})$ is an arbitrary test function and $\mathbb{C}$ is the fourth-rank elasticity tensor. Furthermore,

$$G^{\mathrm{ext}} = \int_{\Omega} \mathbf{w}_{\mathbf{u}} \cdot \mathbf{b}\, \mathrm{d}A + \int_{\partial\Omega_t} \mathbf{w}_{\mathbf{u}} \cdot \bar{\mathbf{t}}\, \mathrm{d}S, \tag{3}$$

where $\mathbf{b}(\mathbf{x})$ denotes the body force field.

Taking into account the symmetry properties of the strain tensor and the elasticity tensor, the weak form (2) can, with the help of Voigt's vector notation, alternatively be expressed as

$$\int_{\Omega} \boldsymbol{\varepsilon}_{\mathrm{V}}\left(\mathbf{w}_{\mathbf{u}}\right) \cdot \mathbf{D}\boldsymbol{\varepsilon}_{\mathrm{V}}(\mathbf{u})\, \mathrm{d}A = G^{\mathrm{ext}}, \tag{4}$$

where

$$\boldsymbol{\varepsilon}_{\mathrm{V}}(\mathbf{u}) = \left[\varepsilon_{xx},\ \varepsilon_{yy},\ 2\varepsilon_{xy}\right]^{\mathrm{T}} = \left[\frac{\partial u_x}{\partial x},\ \frac{\partial u_y}{\partial y},\ \frac{\partial u_x}{\partial y} + \frac{\partial u_y}{\partial x}\right]^{\mathrm{T}}. \tag{5}$$

Furthermore, the elasticity matrix corresponds to

$$\mathbf{D} = \begin{cases} \dfrac{E}{1-\nu^2}\begin{bmatrix} 1 & \nu & 0 \\ \nu & 1 & 0 \\ 0 & 0 & \frac{1-\nu}{2} \end{bmatrix} & \text{(plane stress)} \\ \dfrac{E}{(1+\nu)(1-2\nu)}\begin{bmatrix} 1-\nu & \nu & 0 \\ \nu & 1-\nu & 0 \\ 0 & 0 & \frac{1-2\nu}{2} \end{bmatrix} & \text{(plane strain)} \end{cases}, \tag{6}$$

with Young's modulus E and Poisson's ratio ν.

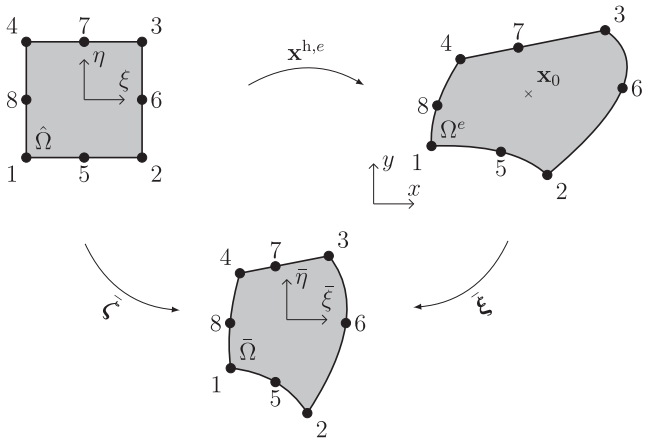

FIGURE 1 | Illustration of the different element domains (reference domain $\hat{\Omega}$, physical domain Ω^e, skew domain $\overline{\Omega}$) and the corresponding mappings (isoparametric map $\mathbf{x}^{\mathrm{h},e}$, see (8); skew map $\overline{\boldsymbol{\xi}}$, see (11); additional map $\overline{\boldsymbol{\zeta}}$, compare [15], not relevant here) for a distorted 8-node element.

In the finite element method, the body Ω is subdivided into n_e finite elements such that

$$\Omega \approx \Omega^{\mathrm{h}} = \bigcup_{e=1}^{n_e} \Omega^e, \tag{7}$$

where the superscript $(\bullet)^{\mathrm{h}}$ indicates an approximation. In the *UQ8** formulation, each element has 8 nodes and can be considered in different domains. As illustrated in Figure 1, an element may be represented not only in the physical domain Ω^e, but also in the reference domain $\hat{\Omega}$ and in the skew domain $\overline{\Omega}$.

The reference domain corresponds to a square with side length 2. The origin of the reference coordinates $\boldsymbol{\xi} = [\xi,\ \eta]^{\mathrm{T}}$ is located at the center of the square. Thus, $\xi,\ \eta \in [-1,\ 1]$. The relationship between the reference domain and the physical domain is established via the isoparametric map

$$\mathbf{x}^{\mathrm{h},e} = \sum_{i=1}^{8} N_i(\boldsymbol{\xi}) \mathbf{X}_i^e, \tag{8}$$

where $N_i(\boldsymbol{\xi})$ are the standard quadratic serendipity shape functions given by

$$\begin{aligned}
N_1(\boldsymbol{\xi}) &= \frac{1}{4}(1-\xi)(1-\eta)(-\xi-\eta-1), & N_2(\boldsymbol{\xi}) &= \frac{1}{4}(1+\xi)(1-\eta)(\xi-\eta-1),\\
N_3(\boldsymbol{\xi}) &= \frac{1}{4}(1+\xi)(1+\eta)(\xi+\eta-1), & N_4(\boldsymbol{\xi}) &= \frac{1}{4}(1-\xi)(1+\eta)(-\xi+\eta-1),\\
N_5(\boldsymbol{\xi}) &= \frac{1}{2}(1-\xi^2)(1-\eta), & N_6(\boldsymbol{\xi}) &= \frac{1}{2}(1+\xi)(1-\eta^2),\\
N_7(\boldsymbol{\xi}) &= \frac{1}{2}(1-\xi^2)(1+\eta), & N_8(\boldsymbol{\xi}) &= \frac{1}{2}(1-\xi)(1-\eta^2),
\end{aligned} \tag{9}$$

and $\mathbf{X}_i^e$ are the physical coordinates of the i-th node.

Accordingly, the Jacobian of the transformation is given by

$$\mathbf{J}^{\mathrm{h},e} = \frac{\partial \mathbf{x}^{\mathrm{h},e}}{\partial \boldsymbol{\xi}} = \sum_{i=1}^{8} \mathbf{X}_i^e \otimes \nabla_{\boldsymbol{\xi}} N_i. \tag{10}$$

An essential component of the *UQ8** formulation is the use of the frame-indifferent skew coordinates (see also [5, 15]). These can be defined via the affine skew map

$$\overline{\boldsymbol{\xi}} = [\overline{\xi},\ \overline{\eta}]^{\mathrm{T}} = \mathbf{J}_0^{-1}\left(\mathbf{x}^{\mathrm{h},e} - \mathbf{x}_0\right). \tag{11}$$

Therein, $\mathbf{x}_0 = \mathbf{x}^{\mathrm{h},e}|_{\boldsymbol{\xi}=\mathbf{0}}$ denotes the position of the element center, and $\mathbf{J}_0 = \mathbf{J}^{\mathrm{h},e}|_{\boldsymbol{\xi}=\mathbf{0}}$ corresponds to the Jacobian evaluated at the center of the element. As can be seen from Figure 1, the skew domain of the element generally differs from the reference domain. However, if an element is undistorted, or more precisely, if the Jacobian of the transformation (10) is constant, the skew domain of the element coincides with the reference domain.

Petrov-Galerkin finite element formulations are characterized by the fact that, in contrast to the usual Bubnov-Galerkin finite element formulations, different ansatz spaces are employed for the approximation of the test and trial functions. Within the *UQ8** formulation, the approximation of the test function is carried out at the element level in the same way as in standard formulations. This means, according to

$$\mathbf{w}_{\mathbf{u}}^{\mathrm{h},e} = \sum_{i=1}^{8} N_i(\boldsymbol{\xi}) \mathbf{W}_{\mathbf{u}i}^{e}, \tag{12}$$

where $\mathbf{W}_{\mathbf{u}i}^{e}$ are the nodal values of the test function. In contrast, the approximation of the trial function (the displacement field) is performed employing so-called metric shape functions $\hat{N}_i^e(\bar{\boldsymbol{\xi}})$ in accordance with

$$\mathbf{u}^{\mathrm{h},e} = \sum_{i=1}^{8} \hat{N}_i^e(\bar{\boldsymbol{\xi}}) \mathbf{U}_i^e, \tag{13}$$

where $\mathbf{U}_i^e$ are the nodal values of the trial function.

At its core, this unusual approximation procedure can be traced back to Rajendran and Liew [2]. The motivation behind this approach is to obtain a formulation capable of accurately reproducing any quadratic displacement field, that is, a displacement field of the form

$$\mathbf{u}(\mathbf{x}) = \mathbf{a}_1 + \mathbf{a}_2\, x + \mathbf{a}_3\, y + \mathbf{a}_4\, x^2 + \mathbf{a}_5\, xy + \mathbf{a}_6\, y^2, \tag{14}$$

where $\mathbf{a}_1$ to $\mathbf{a}_6$ are arbitrary constants, even when the elements employed are severely distorted. This is only possible if the approximation of the displacement field is able to exactly reproduce all monomials appearing in (14), regardless of the element shape. Since this requirement cannot be satisfied when using standard serendipity shape functions (cf. [1]), the *UQ8** formulation employs special shape functions specifically designed to enable this.

In the following, the derivation of these metric shape functions is outlined. Within the framework of the *UQ8** formulation, it is required that the formulation should be able to accurately reproduce any displacement field of the form

$$\mathbf{u}(\bar{\boldsymbol{\xi}}) = \mathbf{b}_1 + \mathbf{b}_2\, \bar{\xi} + \mathbf{b}_3\, \bar{\eta} + \mathbf{b}_4\, \bar{\xi}^2 + \mathbf{b}_5\, \bar{\xi}\bar{\eta} + \mathbf{b}_6\, \bar{\eta}^2 + \mathbf{b}_7\, \bar{\xi}^2\bar{\eta} + \mathbf{b}_8\, \bar{\xi}\bar{\eta}^2, \tag{15}$$

where $\mathbf{b}_1$ to $\mathbf{b}_8$ are arbitrary constants. Note that this requirement also includes (14) due to the affine relationship between the physical coordinates and the skew coordinates, see (11). Since the nodal interpolation formula (13) should be able to reproduce (15),

$$\sum_{i=1}^{8} \hat{N}_i^e(\bar{\boldsymbol{\xi}}) \mathbf{U}_i^e = \mathbf{b}_1 + \mathbf{b}_2\, \bar{\xi} + \mathbf{b}_3\, \bar{\eta} + \mathbf{b}_4\, \bar{\xi}^2 + \mathbf{b}_5\, \bar{\xi}\bar{\eta} + \mathbf{b}_6\, \bar{\eta}^2 + \mathbf{b}_7\, \bar{\xi}^2\bar{\eta} + \mathbf{b}_8\, \bar{\xi}\bar{\eta}^2 \tag{16}$$

must be satisfied. Taking into account the nodal conditions $\mathbf{U}_i^e = \mathbf{u}(\bar{\boldsymbol{\xi}}_i)$ leads to

$$\begin{aligned} &\sum_{i=1}^{8} \hat{N}_i^e(\bar{\boldsymbol{\xi}}) \Big(\mathbf{b}_1 + \mathbf{b}_2\, \bar{\xi}_i + \mathbf{b}_3\, \bar{\eta}_i + \mathbf{b}_4\, \bar{\xi}_i^2 + \mathbf{b}_5\, \bar{\xi}_i\bar{\eta}_i + \mathbf{b}_6\, \bar{\eta}_i^2 + \mathbf{b}_7\, \bar{\xi}_i^2\bar{\eta}_i + \mathbf{b}_8\, \bar{\xi}_i\bar{\eta}_i^2 \Big) \\ &\qquad = \mathbf{b}_1 + \mathbf{b}_2\, \bar{\xi} + \mathbf{b}_3\, \bar{\eta} + \mathbf{b}_4\, \bar{\xi}^2 + \mathbf{b}_5\, \bar{\xi}\bar{\eta} + \mathbf{b}_6\, \bar{\eta}^2 + \mathbf{b}_7\, \bar{\xi}^2\bar{\eta} + \mathbf{b}_8\, \bar{\xi}\bar{\eta}^2, \end{aligned} \tag{17}$$

where $\bar{\xi}_i$ and $\bar{\eta}_i$ denote the skew coordinates of the i-th node. From (17), eight conditions can be derived that must be satisfied individually in order for the equation to hold for arbitrary constants. These conditions can be expressed compactly in matrix-vector notation as

$$\mathbf{P}\hat{\mathbf{n}} = \mathbf{p}(\bar{\xi},\ \bar{\eta}), \tag{18}$$

where

$$\hat{\mathbf{n}} = \left[\hat{N}_1^e,\ \hat{N}_2^e,\ \ldots,\ \hat{N}_8^e\right]^{\mathrm{T}}, \tag{19a}$$

$$\mathbf{p}(\bar{\xi},\ \bar{\eta}) = \left[1,\ \bar{\xi},\ \bar{\eta},\ \bar{\xi}^2,\ \bar{\xi}\bar{\eta},\ \bar{\eta}^2,\ \bar{\xi}^2\bar{\eta},\ \bar{\xi}\bar{\eta}^2\right]^{\mathrm{T}}, \tag{19b}$$

$$\mathbf{P} = \left[\mathbf{p}(\bar{\xi}_1,\ \bar{\eta}_1),\ \mathbf{p}(\bar{\xi}_2,\ \bar{\eta}_2),\ \ldots,\ \mathbf{p}(\bar{\xi}_8,\ \bar{\eta}_8)\right]. \tag{19c}$$

The metric shape functions can be determined by solving the system of linear equations (18). In general, these metric shape functions must be determined for each element individually. This is possible as long as there are no coincident nodes. Note that the metric shape functions are identical to the serendipity shape functions (9) when the Jacobian of the transformation (10) is constant.

Apart from the specific approximation of the displacement field, the *UQ8** formulation does not differ from standard finite element formulations. The approximations (12) and (13) can equivalently be expressed in matrix-vector notation as

$$\mathbf{w}_{\mathbf{u}}^{\mathrm{h},e} = \mathbf{N}^e\mathbf{W}_{\mathbf{u}}^e\,, \quad \mathbf{u}^{\mathrm{h},e} = \hat{\mathbf{N}}^e\mathbf{U}^e, \tag{20}$$

with the standard matrix of shape functions

$$\mathbf{N}^e = \left[N_1\mathbf{I},\ N_2\mathbf{I},\ \ldots,\ N_8\mathbf{I}\right] \tag{21}$$

and the matrix of metric shape functions

$$\hat{\mathbf{N}}^e = \left[\hat{N}_1^e\mathbf{I},\ \hat{N}_2^e\mathbf{I},\ \ldots,\ \hat{N}_8^e\mathbf{I}\right], \tag{22}$$

where $\mathbf{I}$ denotes the 2×2 identity matrix. Moreover, $\mathbf{W}_{\mathbf{u}}^e$ and $\mathbf{U}^e$ are the vectors of the nodal values, where, for example,

$$\mathbf{U}^e = \left[U_{x_1}^e,\ U_{y_1}^e,\ U_{x_2}^e,\ U_{y_2}^e,\ \ldots,\ U_{x_8}^e,\ U_{y_8}^e\right]. \tag{23}$$

In a similar fashion, the strain tensors in Voigt's vector notation appearing in (4) can be expressed compactly as

$$\boldsymbol{\varepsilon}_{\mathrm{V}}\left(\mathbf{w}_{\mathbf{u}}^{\mathrm{h},e}\right) = \mathbf{B}^e\mathbf{W}_{\mathbf{u}}^e\,, \quad \boldsymbol{\varepsilon}_{\mathrm{V}}\left(\mathbf{u}^{\mathrm{h},e}\right) = \hat{\mathbf{B}}^e\mathbf{U}^e, \tag{24}$$

with the standard strain-displacement matrix $\mathbf{B}^e$ and the metric strain-displacement matrix $\hat{\mathbf{B}}^e$. Both strain-displacement matrices contain derivatives of the respective shape functions with respect to the physical coordinates. For the serendipity shape functions, these derivatives can be determined according to

$$\nabla_{\mathbf{x}} N_i = (\mathbf{J}^{\mathrm{h},e})^{-\mathrm{T}}\nabla_{\boldsymbol{\xi}} N_i, \tag{25}$$

whereas the corresponding derivatives of the metric shape functions can be computed via

$$\nabla_{\mathbf{x}}\hat{N}_i^e = \mathbf{J}_0^{-\mathrm{T}}\nabla_{\bar{\boldsymbol{\xi}}}\hat{N}_i^e. \tag{26}$$

Following the standard procedure in the finite element method, an element stiffness matrix and an element load vector can be defined at the element level based on the relationships introduced above. By introducing $\mathbb{A}$ as the assembly operator, the global stiffness matrix can then be defined via

$$\tilde{\mathbf{K}} = \bigwedge_{e=1}^{n_e}\left(\int_{\Omega^e}(\mathbf{B}^e)^{\mathrm{T}}\,\mathbf{D}\hat{\mathbf{B}}^e\ \mathrm{d}A\right). \tag{27}$$

Note that, in contrast to standard formulations, the global stiffness matrix is generally unsymmetric for the *UQ8** formulation. After the assembly procedure, the resulting system of equations can be expressed in the usual form as

$$\tilde{\mathbf{K}}\mathbf{U} = \mathbf{F}^{\mathrm{ext}}, \tag{28}$$

with the global nodal displacement vector $\mathbf{U}$ and the global load vector $\mathbf{F}^{\mathrm{ext}}$. Note that, for the formulation considered in this work, the global load vector results from inserting (12) into (3) and is therefore identical to that of standard Bubnov-Galerkin formulations.

3 | Extension to Elastodynamics

In this section, three different approaches are presented that show how Petrov-Galerkin finite element formulations – initially developed for the linear elastostatic case – can be extended to the dynamic regime. These approaches are applied specifically to the *UQ8** formulation from Section 2; however, the underlying ideas can, in principle, be transferred to other formulations as well.

In contrast to the elastostatic case, it is now assumed that the deformation of the continuum body Ω also depends on time $t \in \mathcal{I} = [0,\ T]$, where $T \in \mathbb{R}^+$ denotes the total time. Furthermore, the velocity field $\mathbf{v}(\mathbf{x}, t)$ is introduced as the time derivative of the displacement field, that is,

$$\mathbf{v}(\mathbf{x}, t) = \frac{\mathrm{d}}{\mathrm{d}t}\mathbf{u}(\mathbf{x}, t) = \dot{\mathbf{u}}(\mathbf{x}, t). \tag{29}$$

In addition, it is assumed that the initial displacement field $\mathbf{u}_0 = \mathbf{u}(\mathbf{x},\ 0)$ and the initial velocity field $\mathbf{v}_0 = \mathbf{v}(\mathbf{x},\ 0)$ are prescribed.

3.1 | The Conventional Approach

The first approach, referred to as the *conventional approach* in the following, reflects the usual procedure for extending standard Bubnov-Galerkin formulations to elastodynamics. It is presented here to demonstrate that techniques developed for Bubnov-Galerkin formulations cannot always be directly transferred to Petrov-Galerkin formulations.

For this approach, the weak form

$$\int_\Omega \mathbf{w}_\mathbf{u} \cdot \rho\ddot{\mathbf{u}}\, \mathrm{d}A + \int_\Omega \boldsymbol{\varepsilon}\left(\mathbf{w}_\mathbf{u}\right) : \mathbb{C} : \boldsymbol{\varepsilon}(\mathbf{u})\, \mathrm{d}A = G^{\mathrm{ext}} \tag{30}$$

is taken as a starting point. Compared to the weak form of elastostatics (2), the present weak form now additionally includes the inertia term, with the mass density $\rho \in \mathbb{R}^+$.

3.1.1 | Discretization in Space

In a first step, the spatial discretization of the weak form (30) is carried out. As in the elastostatic formulation (cf. Section 2), the test and trial functions are approximated at the element level employing different ansatz functions. Building on the elastostatic formulation, the approximations

$$\mathbf{w}_\mathbf{u}^{\mathrm{h},e} = \mathbf{N}^e \mathbf{W}_\mathbf{u}^e\,, \quad \mathbf{u}^{\mathrm{h},e} = \hat{\mathbf{N}}^e \mathbf{U}^e\,, \quad \dot{\mathbf{u}}^{\mathrm{h},e} = \hat{\mathbf{N}}^e \dot{\mathbf{U}}^e\,, \quad \ddot{\mathbf{u}}^{\mathrm{h},e} = \hat{\mathbf{N}}^e \ddot{\mathbf{U}}^e \tag{31}$$

represent the most natural choice in this context. Substituting these approximations into the weak form (30) and subsequent assembly of the element contributions leads to

$$\mathbf{W}_\mathbf{u} \cdot (\tilde{\mathbf{M}}\ddot{\mathbf{U}} + \tilde{\mathbf{K}}\mathbf{U}) = \mathbf{W}_\mathbf{u} \cdot \mathbf{F}^{\mathrm{ext}} \tag{32}$$

at the global level. Therein, $\tilde{\mathbf{K}}$ corresponds to the global stiffness matrix (27), and $\tilde{\mathbf{M}}$ is the global mass matrix given by

$$\tilde{\mathbf{M}} = \bigwedge_{e=1}^{n_e} \left(\int_{\Omega^e} (\mathbf{N}^e)^{\mathrm{T}}\, \rho \hat{\mathbf{N}}^e\, \mathrm{d}A \right). \tag{33}$$

Note that both matrices are generally unsymmetric. In the following, these matrices are also collectively referred to as unsymmetric system matrices. Due to the arbitrariness of the test functions, (32) may also be written as

$$\tilde{\mathbf{M}}\ddot{\mathbf{U}} + \tilde{\mathbf{K}}\mathbf{U} = \mathbf{F}^{\mathrm{ext}}. \tag{34}$$

This system of equations represents the semi-discrete equations of motion pertaining to the conventional approach.

3.1.2 | Discretization in Time

We now turn to the temporal discretization of the semi-discrete equations of motion. To this end, the system of second-order ordinary differential equations (34) is reformulated to convert it into an equivalent system of first-order

equations. More precisely, by introducing the nodal velocities $\mathbf{V}$ as independent variables, it is possible to rewrite (34) equivalently as

$$\dot{\mathbf{U}} = \mathbf{V}, \tag{35a}$$

$$\tilde{\mathbf{M}}\dot{\mathbf{V}} + \tilde{\mathbf{K}}\mathbf{U} = \mathbf{F}^{\text{ext}}. \tag{35b}$$

Various time integration schemes are available for the numerical solution of equations of this type. A common method that we favor in this case is the implicit midpoint rule. For this one-step method, the interval $\mathcal{I}$ is divided into subintervals $[t_n,\ t_{n+1}] \subset \mathcal{I}$. It is assumed that the nodal values of the displacement field and the velocity field are known at time t_n and sought at time t_{n+1}. Applying the implicit midpoint rule to (35) yields

$$\mathbf{U}_{n+1} - \mathbf{U}_n = \Delta t\ \mathbf{V}_{n+\frac{1}{2}}, \tag{36a}$$

$$\tilde{\mathbf{M}}\big(\mathbf{V}_{n+1} - \mathbf{V}_n\big) + \Delta t\ \tilde{\mathbf{K}}\mathbf{U}_{n+\frac{1}{2}} = \Delta t\ \mathbf{F}^{\text{ext}}\Big(t_{n+\frac{1}{2}}\Big), \tag{36b}$$

where the fields at time t_n are denoted by $(\bullet)_n$ and at time t_{n+1} by $(\bullet)_{n+1}$. Furthermore, $(\bullet)_{n+\frac{1}{2}} = \frac{1}{2}\big[(\bullet)_n + (\bullet)_{n+1}\big]$ is the average value and $\Delta t = t_{n+1} - t_n$ denotes the time step size.

To simplify the numerical solution of these equations, it is convenient to rewrite Equation (36a) in the form

$$\mathbf{V}_{n+1} = \frac{2}{\Delta t}\big(\mathbf{U}_{n+1} - \mathbf{U}_n\big) - \mathbf{V}_n. \tag{37}$$

Substituting this relationship into Equation (36b) ultimately yields

$$\tilde{\mathbf{M}}\Big(\frac{2}{\Delta t^2}\big(\mathbf{U}_{n+1} - \mathbf{U}_n\big) - \frac{2}{\Delta t}\mathbf{V}_n\Big) + \tilde{\mathbf{K}}\mathbf{U}_{n+\frac{1}{2}} = \mathbf{F}^{\text{ext}}\Big(t_{n+\frac{1}{2}}\Big). \tag{38}$$

In this representation, the sought nodal displacements $\mathbf{U}_{n+1}$ can be obtained directly from Equation (38). The nodal velocities $\mathbf{V}_{n+1}$ then follow from Equation (37).

Remark 1. For the temporal discretization of linear elastodynamic problems, Newmark's method [21] is often used instead of the implicit midpoint rule. For Petrov-Galerkin formulations, the corresponding procedure can be stated as

$$\mathbf{U}_{n+1} = \mathbf{U}_n + \Delta t\ \mathbf{V}_n + \Delta t^2\Big(\Big(\frac{1}{2} - \beta\Big)\mathbf{A}_n + \beta\mathbf{A}_{n+1}\Big), \tag{39a}$$

$$\mathbf{V}_{n+1} = \mathbf{V}_n + \Delta t\big((1-\gamma)\mathbf{A}_n + \gamma\mathbf{A}_{n+1}\big), \tag{39b}$$

$$\tilde{\mathbf{M}}\mathbf{A}_{n+1} + \tilde{\mathbf{K}}\mathbf{U}_{n+1} = \mathbf{F}^{\text{ext}}_{n+1}, \tag{39c}$$

where $0 \leq \beta \leq \frac{1}{2}$ and $0 \leq \gamma \leq 1$ are two scalar parameters that can be used to control the numerical properties of the method (see, e.g., [22]).

It is well known that Newmark's method is unconditionally stable when the system matrices are symmetric, and the associated scalar parameters are chosen as $\gamma \geq \frac{1}{2}$ and $\beta \geq \frac{1}{2}\gamma$. In particular, for $\beta = \frac{1}{4}$ and $\gamma = \frac{1}{2}$, Newmark's method is capable of conserving the total energy. However, when simulations are performed with unsymmetric system matrices, numerical instabilities may occur regardless of the time discretization scheme (see [20] and the numerical results in Section 4). An explanation for this phenomenon is provided in the following section.

Independent of this, it is worth noting that certain relationships between different time discretization schemes, which are already well-known for Bubnov-Galerkin formulations, also appear to hold for Petrov-Galerkin formulations (cf. Appendix A).

3.1.3 | Analysis at the Energy Level

The numerical investigations (see Section 4) demonstrate that the conventional approach is not suitable for the dynamic extension of Petrov-Galerkin finite element formulations. Specifically, simulations using this approach tend to be highly

unstable. This can be attributed to the fact that the global energy balance is violated already at the semi-discrete level (cf. [20]). For the present formulation, this can be readily demonstrated.

The total energy of a mechanical system corresponds to the sum of the kinetic energy

$$T = \frac{1}{2}\int_{\Omega} \rho \dot{\mathbf{u}} \cdot \dot{\mathbf{u}} \, \mathrm{d}A \tag{40}$$

and the potential energy

$$V = \frac{1}{2}\int_{\Omega} \boldsymbol{\varepsilon}(\mathbf{u}) : \mathbb{C} : \boldsymbol{\varepsilon}(\mathbf{u}) \, \mathrm{d}A. \tag{41}$$

Accordingly, the total energy of the semi-discrete formulation is given by

$$E = \frac{1}{2}\dot{\mathbf{U}} \cdot \hat{\mathbf{M}}\dot{\mathbf{U}} + \frac{1}{2}\mathbf{U} \cdot \hat{\mathbf{K}}\mathbf{U}, \tag{42}$$

where the metric system matrices

$$\hat{\mathbf{M}} = \bigwedge_{e=1}^{n_e} \left(\int_{\Omega^e} (\hat{\mathbf{N}}^e)^{\mathrm{T}} \, \rho \hat{\mathbf{N}}^e \, \mathrm{d}A \right), \quad \hat{\mathbf{K}} = \bigwedge_{e=1}^{n_e} \left(\int_{\Omega^e} (\hat{\mathbf{B}}^e)^{\mathrm{T}} \, \mathbf{D} \hat{\mathbf{B}}^e \, \mathrm{d}A \right), \tag{43}$$

result from inserting the spatial approximation formulas (31) into (40) and (41), respectively, and the subsequent assembly of the element contributions. Note that the metric system matrices are symmetric.

A mechanical system must satisfy the global energy balance

$$\dot{E} = P^{\mathrm{ext}}, \tag{44}$$

where P^{ext} denotes the power of the external forces given by

$$P^{\mathrm{ext}} = \int_{\Omega} \dot{\mathbf{u}} \cdot \mathbf{b} \, \mathrm{d}A + \int_{\partial\Omega_t} \dot{\mathbf{u}} \cdot \bar{\mathbf{t}} \, \mathrm{d}S. \tag{45}$$

For the present semi-discrete formulation, differentiating the total energy (42) with respect to time yields

$$\dot{E} = \dot{\mathbf{U}} \cdot \hat{\mathbf{M}}\ddot{\mathbf{U}} + \dot{\mathbf{U}} \cdot \hat{\mathbf{K}}\mathbf{U}. \tag{46}$$

The balance law (44) implies conservation of energy in the case of vanishing external loads, that is, $\dot{E} = 0$ for $P^{\mathrm{ext}} = 0$. In the next step, we examine whether the semi-discrete formulation (34) satisfies this condition. To this end, we set $\mathbf{F}^{\mathrm{ext}} = \mathbf{0}$ and take the scalar product of (34) with $\dot{\mathbf{U}}$ to obtain

$$\dot{\mathbf{U}} \cdot (\tilde{\mathbf{M}}\ddot{\mathbf{U}} + \tilde{\mathbf{K}}\mathbf{U}) = 0. \tag{47}$$

Subtracting (47) from the right-hand side of (46) results in

$$\dot{E} = \dot{\mathbf{U}} \cdot (\hat{\mathbf{M}} - \tilde{\mathbf{M}})\ddot{\mathbf{U}} + \dot{\mathbf{U}} \cdot (\hat{\mathbf{K}} - \tilde{\mathbf{K}})\mathbf{U}. \tag{48}$$

For regular meshes, the right-hand side of the last equation vanishes, since the two bracketed expressions reduce to the zero matrix due to the coincidence of the serendipity and the metric shape functions (see Section 2). Accordingly, conservation of total energy, that is, $\dot{E} = 0$, is ensured in this case. For distorted meshes, however, the two bracketed expressions in (48) do not reduce to the zero matrix, and the semi-discrete formulation therefore fails to conserve the total energy in general.

3.2 | The Approach by Wang and Hillman

The second approach considered in this work builds on Wang and Hillman [20], who propose a modified time integration scheme for Petrov-Galerkin formulations. The method is developed in the context of the reproducing kernel collocation

method (RKCM) and the reproducing kernel finite-volume method (RKFM) – two methods that lead to unsymmetric system matrices. In the present contribution, we apply this approach to the mesh-distortion-insensitive *UQ8** formulation from Section 2.

Wang and Hillman [20] recognized that the numerically unstable behavior of Petrov-Galerkin formulations, extended to dynamics in a conventional manner, can be attributed to the fact that such formulations do not, in general, satisfy the global energy balance at the semi-discrete level (cf. Section 3.1.3). As a remedy, Wang and Hillman [20] propose modifying the time integration method so that the global energy balance is satisfied at the fully-discrete level.

Integrating the global energy balance (44) over an arbitrary time interval $[t_n,\ t_{n+1}] \subset \mathcal{I}$ yields the discrete global energy balance

$$E_{n+1} - E_n = \int_{t_n}^{t_{n+1}} P^{\text{ext}}\, \mathrm{d}t. \tag{49}$$

Within the framework of the *UQ8** formulation, employing the same spatial discretization as in the conventional approach (see Section 3.1.1), the total energy at the two different points in time can be computed via

$$E_{n+1} = \frac{1}{2}\mathbf{V}_{n+1} \cdot \hat{\mathbf{M}}\mathbf{V}_{n+1} + \frac{1}{2}\mathbf{U}_{n+1} \cdot \hat{\mathbf{K}}\mathbf{U}_{n+1}, \tag{50a}$$

$$E_n = \frac{1}{2}\mathbf{V}_n \cdot \hat{\mathbf{M}}\mathbf{V}_n + \frac{1}{2}\mathbf{U}_n \cdot \hat{\mathbf{K}}\mathbf{U}_n. \tag{50b}$$

For the right-hand side of (49), Wang and Hillman [20] propose to use the approximation

$$\int_{t_n}^{t_{n+1}} P^{\text{ext}}\, \mathrm{d}t = \left(\mathbf{U}_{n+1} - \mathbf{U}_n\right) \cdot \mathbf{F}^{\text{ext}}_{n+\frac{1}{2}}. \tag{51}$$

Accordingly, to satisfy the discrete global energy balance (49),

$$\left(\mathbf{V}_{n+1} - \mathbf{V}_n\right) \cdot \hat{\mathbf{M}}\mathbf{V}_{n+\frac{1}{2}} + \left(\mathbf{U}_{n+1} - \mathbf{U}_n\right) \cdot \left(\hat{\mathbf{K}}\mathbf{U}_{n+\frac{1}{2}} - \mathbf{F}^{\text{ext}}_{n+\frac{1}{2}}\right) = 0 \tag{52}$$

must hold. To meet this requirement, Wang and Hillman [20] propose a modification of the conventional Newmark method (39). Since simulations using conventional approaches typically lead to an energy blow-up (cf. Section 4.1.2), the central idea of their method is to adjust the parameter γ in Newmark's velocity update formula (39b) so that the discrete global energy balance (49) is satisfied. Since the value of this parameter must be recomputed in every time step, it is denoted by γ_n in the following.

In the present work, we choose the Newmark parameter $\beta = \frac{1}{4}$ from the outset. Then, according to Wang and Hillman [20], $\mathbf{U}_{n+1}$ and $\mathbf{A}_{n+1}$ are first determined, as in the conventional Newmark method, by solving

$$\mathbf{U}_{n+1} = \mathbf{U}_n + \Delta t\ \mathbf{V}_n + \frac{\Delta t^2}{4}\left(\mathbf{A}_n + \mathbf{A}_{n+1}\right), \tag{53a}$$

$$\tilde{\mathbf{M}}\mathbf{A}_{n+1} + \tilde{\mathbf{K}}\mathbf{U}_{n+1} = \mathbf{F}^{\text{ext}}_{n+1}. \tag{53b}$$

Subsequently, a suitable value for the scalar parameter γ_n is computed such that the discrete global energy balance is satisfied. To this end, (39b) is substituted into (52). The two solutions of the resulting equation are

$$\gamma_{n_{1,2}} = \frac{-b \pm \sqrt{b^2 - 4ac}}{2a}, \tag{54}$$

where

$$a = \frac{1}{2}\Delta t^2\left(\mathbf{A}_{n+1} - \mathbf{A}_n\right) \cdot \hat{\mathbf{M}}\left(\mathbf{A}_{n+1} - \mathbf{A}_n\right), \tag{55a}$$

$$b = \Delta t\left(\mathbf{V}_n + \Delta t\ \mathbf{A}_n\right) \cdot \hat{\mathbf{M}}\left(\mathbf{A}_{n+1} - \mathbf{A}_n\right), \tag{55b}$$

$$c = \frac{1}{2}\Delta t\ \mathbf{A}_n \cdot \hat{\mathbf{M}}\left(2\mathbf{V}_n + \Delta t\ \mathbf{A}_n\right) + \left(\mathbf{U}_{n+1} - \mathbf{U}_n\right) \cdot \left(\hat{\mathbf{K}}\mathbf{U}_{n+\frac{1}{2}} - \mathbf{F}^{\text{ext}}_{n+\frac{1}{2}}\right). \tag{55c}$$

In theory, the discrete global energy balance is satisfied for both solutions. Therefore, a strategy must be developed to decide which of the two solutions is used for the subsequent computation of the nodal velocity vector. The strategy adopted here is to always select the value that is closest to the conventional value $\gamma = \frac{1}{2}$. This finally enables the computation of the nodal velocity vector, analogous to (39b), via

$$\mathbf{V}_{n+1} = \mathbf{V}_n + \Delta t\left((1-\gamma_n)\mathbf{A}_n + \gamma_n \mathbf{A}_{n+1}\right). \tag{56}$$

In Section 4, the results of a numerical example computed with this approach are presented in detail. These results indicate that this approach is not generally suitable for the dynamic extension of Petrov-Galerkin formulations. More precisely, within this method it is possible that the case $b^2 - 4ac < 0$ occurs, which implies that $\gamma_{n_{1,2}}$ are no longer real-valued. Although the possibility of such an occurrence was already mentioned in Wang and Hillman [20], the problem appears to be significantly more severe for the *UQ8** formulation than for the formulations examined in their work.

3.3 | A Novel Approach

In this section, we present a novel approach that was developed from the outset with the objective of satisfying the global energy balance. A key distinction from the two approaches considered earlier is that the velocity field $\mathbf{v}$ is introduced as an independent variable from the beginning. In this context, we propose using the weak form

$$\int_\Omega \boldsymbol{\varepsilon}\left(\mathbf{w}_\mathbf{v}\right) : \mathbb{C} : \left(\boldsymbol{\varepsilon}(\dot{\mathbf{u}}) - \boldsymbol{\varepsilon}(\mathbf{v})\right) \mathrm{d}A = 0, \tag{57a}$$

$$\int_\Omega \mathbf{w}_\mathbf{u} \cdot \rho\dot{\mathbf{v}}\, \mathrm{d}A + \int_\Omega \boldsymbol{\varepsilon}\left(\mathbf{w}_\mathbf{u}\right) : \mathbb{C} : \boldsymbol{\varepsilon}(\mathbf{u})\, \mathrm{d}A = G^{\text{ext}}. \tag{57b}$$

Here, $\mathbf{w}_\mathbf{v}$ is an additional arbitrary test function and G^{ext} is given by (3). Accordingly, in this approach, the kinematic relation between the displacement field and the velocity field (29) is not established directly, but rather imposed at the strain level through (57a). Note that for purely static applications ($\rho = 0$), (57b) boils down to the weak form (2) underlying the *UQ8** formulation as described in Section 2.

It is possible to show at the continuum level that the weak form (57) includes the global energy balance (44). Due to the arbitrariness of the test functions, it is admissible to substitute $\mathbf{w}_\mathbf{u} = \mathbf{v}$ and $\mathbf{w}_\mathbf{v} = \mathbf{u}$ in (57), which gives

$$\int_\Omega \boldsymbol{\varepsilon}(\mathbf{u}) : \mathbb{C} : \left(\boldsymbol{\varepsilon}(\dot{\mathbf{u}}) - \boldsymbol{\varepsilon}(\mathbf{v})\right) \mathrm{d}A = 0, \tag{58a}$$

$$\int_\Omega \mathbf{v} \cdot \rho\dot{\mathbf{v}}\, \mathrm{d}A + \int_\Omega \boldsymbol{\varepsilon}(\mathbf{v}) : \mathbb{C} : \boldsymbol{\varepsilon}(\mathbf{u})\, \mathrm{d}A = P^{\text{ext}}. \tag{58b}$$

Here, P^{ext} again denotes the power of the external forces given by

$$P^{\text{ext}} = \int_\Omega \mathbf{v} \cdot \mathbf{b}\, \mathrm{d}A + \int_{\partial\Omega_t} \mathbf{v} \cdot \bar{\mathbf{t}}\, \mathrm{d}S. \tag{59}$$

Taking into account the major symmetry of the elasticity tensor, it is possible to rearrange (58a) to

$$\int_\Omega \boldsymbol{\varepsilon}(\mathbf{v}) : \mathbb{C} : \boldsymbol{\varepsilon}(\mathbf{u})\, \mathrm{d}A = \int_\Omega \boldsymbol{\varepsilon}(\mathbf{u}) : \mathbb{C} : \boldsymbol{\varepsilon}(\dot{\mathbf{u}})\, \mathrm{d}A. \tag{60}$$

Using this relation, (58b) can be rewritten as

$$\int_\Omega \mathbf{v} \cdot \rho\dot{\mathbf{v}}\, \mathrm{d}A + \int_\Omega \boldsymbol{\varepsilon}(\mathbf{u}) : \mathbb{C} : \boldsymbol{\varepsilon}(\dot{\mathbf{u}})\, \mathrm{d}A = P^{\text{ext}}. \tag{61}$$

As the total energy can be expressed in the form

$$E = \frac{1}{2}\int_\Omega \mathbf{v}\cdot\rho\mathbf{v}\,\mathrm{d}A + \frac{1}{2}\int_\Omega \boldsymbol{\varepsilon}(\mathbf{u}) : \mathbb{C} : \boldsymbol{\varepsilon}(\mathbf{u})\,\mathrm{d}A, \tag{62}$$

it follows that (61) corresponds to $\dot{E} = P^{\mathrm{ext}}$. Accordingly, the proposed weak form includes the global energy balance and thus provides a good starting point for the derivation of a stable numerical formulation.

3.3.1 | Discretization in Space

We now extend the underlying static finite element formulation *UQ8** to the dynamic regime by specifying the approximations of the occurring fields in the weak form (57). To this end, we propose using

$$\begin{aligned}
\mathbf{w}_{\mathbf{u}}^{\mathrm{h},e} &= \mathbf{N}^e\mathbf{W}_{\mathbf{u}}^e\,, & \mathbf{u}^{\mathrm{h},e} &= \hat{\mathbf{N}}^e\mathbf{U}^e\,, & \dot{\mathbf{u}}^{\mathrm{h},e} &= \hat{\mathbf{N}}^e\dot{\mathbf{U}}^e\,,\\
\mathbf{w}_{\mathbf{v}}^{\mathrm{h},e} &= \hat{\mathbf{N}}^e\mathbf{W}_{\mathbf{v}}^e\,, & \mathbf{v}^{\mathrm{h},e} &= \mathbf{N}^e\mathbf{V}^e\,, & \dot{\mathbf{v}}^{\mathrm{h},e} &= \mathbf{N}^e\dot{\mathbf{V}}^e
\end{aligned} \tag{63}$$

as an approximation on the element level. Accordingly, the displacement and velocity related fields are approximated in a "cross-wise" manner. More precisely, the test function of the velocity field $\mathbf{w}_{\mathbf{v}}$ is approximated using the same ansatz functions as those employed for the trial functions $\mathbf{u}$ and $\dot{\mathbf{u}}$, and vice versa.

Substituting the proposed spatial discretization (63) into the weak form (57) yields, at the system level, the semi-discrete equations

$$\mathbf{W}_{\mathbf{v}}\cdot\left(\hat{\mathbf{K}}\dot{\mathbf{U}} - \tilde{\mathbf{K}}^{\mathrm{T}}\mathbf{V}\right) = 0, \tag{64a}$$

$$\mathbf{W}_{\mathbf{u}}\cdot(\mathbf{M}\dot{\mathbf{V}} + \tilde{\mathbf{K}}\mathbf{U}) = \mathbf{W}_{\mathbf{u}}\cdot\mathbf{F}^{\mathrm{ext}}, \tag{64b}$$

where the definitions of $\tilde{\mathbf{K}}$ and $\hat{\mathbf{K}}$ are given in (27) and (43), respectively. Furthermore, $\mathbf{M}$ corresponds to the standard symmetric mass matrix, which can be defined via

$$\mathbf{M} = \bigwedge_{e=1}^{n_e}\left(\int_{\Omega^e}(\mathbf{N}^e)^{\mathrm{T}}\,\rho\mathbf{N}^e\,\mathrm{d}A\right). \tag{65}$$

Next, it is shown that the semi-discrete formulation retains the energy consistency of the underlying continuous formulation. To this end, note that the total energy takes the form

$$E = \frac{1}{2}\mathbf{V}\cdot\mathbf{M}\mathbf{V} + \frac{1}{2}\mathbf{U}\cdot\hat{\mathbf{K}}\mathbf{U} \tag{66}$$

for the present semi-discrete formulation. This results from inserting the spatial approximation formulas (63) into (62). It is worth noting that here, in contrast to (42), the standard consistent mass matrix $\mathbf{M}$ appears in the kinetic energy term rather than the metric mass matrix $\hat{\mathbf{M}}$. Energy consistency is now demonstrated by choosing the admissible nodal values $\mathbf{W}_{\mathbf{v}} = \mathbf{U}$ and $\mathbf{W}_{\mathbf{u}} = \mathbf{V}$ in (64), which yields

$$\mathbf{U}\cdot\left(\hat{\mathbf{K}}\dot{\mathbf{U}} - \tilde{\mathbf{K}}^{\mathrm{T}}\mathbf{V}\right) = 0, \tag{67a}$$

$$\mathbf{V}\cdot(\mathbf{M}\dot{\mathbf{V}} + \tilde{\mathbf{K}}\mathbf{U}) = \mathbf{V}\cdot\mathbf{F}^{\mathrm{ext}}. \tag{67b}$$

Adding the last two equations leads to

$$\mathbf{V}\cdot\mathbf{M}\dot{\mathbf{V}} + \mathbf{U}\cdot\hat{\mathbf{K}}\dot{\mathbf{U}} = \mathbf{V}\cdot\mathbf{F}^{\mathrm{ext}}. \tag{68}$$

The last equation shows the fulfillment of the balance law for the total energy, $\dot{E} = P^{\mathrm{ext}}$, where $P^{\mathrm{ext}} = \mathbf{V}\cdot\mathbf{F}^{\mathrm{ext}}$ results from (59) by substituting the ansatz for the velocity from (63).

Remark 2. Taking into account the arbitrariness of the nodal values associated with the test functions, the semi-discrete equations of motion resulting from (64) can be written in the form

$$\begin{bmatrix} \hat{\mathbf{K}} & \mathbf{0} \\ \mathbf{0} & \mathbf{M} \end{bmatrix} \begin{bmatrix} \dot{\mathbf{U}} \\ \dot{\mathbf{V}} \end{bmatrix} = \begin{bmatrix} \mathbf{0} & \tilde{\mathbf{K}}^{\mathrm{T}} \\ -\tilde{\mathbf{K}} & \mathbf{0} \end{bmatrix} \begin{bmatrix} \mathbf{U} \\ \mathbf{V} \end{bmatrix} + \begin{bmatrix} \mathbf{0} \\ \mathbf{F}^{\mathrm{ext}} \end{bmatrix}. \tag{69}$$

These equations fit into the framework of port-Hamiltonian (pH) systems (see, for example, [23, 24]). Introducing the state vector $\mathbf{Q}^{\mathrm{T}} = [\mathbf{U}^{\mathrm{T}}, \mathbf{V}^{\mathrm{T}}]$, (69) can be written in the characteristic pH form $\mathbf{E}\dot{\mathbf{Q}} = \mathbf{J}\mathbf{Z} + \mathbf{G}\mathbf{h}$, where $\mathbf{E}^{\mathrm{T}}\mathbf{Z} = \nabla E(\mathbf{Q})$. The last equation implies $\mathbf{Z} = \mathbf{Q}$, where the symmetry of the descriptor matrix $\mathbf{E}$ has been taken into account. Moreover, $\mathbf{h} = \mathbf{F}^{\mathrm{ext}}$ can be viewed as a vector of control inputs with associated outputs defined by $\mathbf{Y} = \mathbf{G}^{\mathrm{T}}\mathbf{Z} = \mathbf{V}$. The skew-symmetry of the structure matrix $\mathbf{J}$ is a characteristic feature of lossless pH systems and furthermore confirms the energy consistency of the present semi-discrete formulation.

3.3.2 | Discretization in Time

As in the conventional approach, the implicit midpoint rule is again employed for time integration. Applying it to the system of differential equations (64) yields, in a first step,

$$\mathbf{W}_{\mathbf{v}} \cdot \left(\hat{\mathbf{K}} \left(\mathbf{U}_{n+1} - \mathbf{U}_n \right) - \Delta t \, \tilde{\mathbf{K}}^{\mathrm{T}} \mathbf{V}_{n+\frac{1}{2}} \right) = 0, \tag{70a}$$

$$\mathbf{W}_{\mathbf{u}} \cdot \left(\mathbf{M} \left(\mathbf{V}_{n+1} - \mathbf{V}_n \right) + \Delta t \, \tilde{\mathbf{K}} \mathbf{U}_{n+\frac{1}{2}} \right) = \Delta t \, \mathbf{W}_{\mathbf{u}} \cdot \mathbf{F}^{\mathrm{ext}} \left(t_{n+\frac{1}{2}} \right). \tag{70b}$$

The choice of the time integration method is motivated by the objective to satisfy the discrete global energy balance

$$E_{n+1} - E_n = \int_{t_n}^{t_{n+1}} P^{\mathrm{ext}} \, \mathrm{d}t \tag{71}$$

and therefore to ensure stable numerical simulations. For the present formulation, the total energy at time t_{n+1} and at time t_n is given by

$$E_{n+1} = \frac{1}{2} \mathbf{V}_{n+1} \cdot \mathbf{M} \mathbf{V}_{n+1} + \frac{1}{2} \mathbf{U}_{n+1} \cdot \hat{\mathbf{K}} \mathbf{U}_{n+1}, \tag{72a}$$

$$E_n = \frac{1}{2} \mathbf{V}_n \cdot \mathbf{M} \mathbf{V}_n + \frac{1}{2} \mathbf{U}_n \cdot \hat{\mathbf{K}} \mathbf{U}_n. \tag{72b}$$

Furthermore, evaluating the right-hand side of (71) using the implicit midpoint rule yields

$$\int_{t_n}^{t_{n+1}} P^{\mathrm{ext}} \, \mathrm{d}t = \Delta t \, \mathbf{V}_{n+\frac{1}{2}} \cdot \mathbf{F}^{\mathrm{ext}} \left(t_{n+\frac{1}{2}} \right). \tag{73}$$

Thus, the discrete global energy balance (71) can also be expressed as

$$\left(\mathbf{V}_{n+1} - \mathbf{V}_n \right) \cdot \mathbf{M} \mathbf{V}_{n+\frac{1}{2}} + \left(\mathbf{U}_{n+1} - \mathbf{U}_n \right) \cdot \hat{\mathbf{K}} \mathbf{U}_{n+\frac{1}{2}} = \Delta t \, \mathbf{V}_{n+\frac{1}{2}} \cdot \mathbf{F}^{\mathrm{ext}} \left(t_{n+\frac{1}{2}} \right). \tag{74}$$

Next, it shall be shown that this balance equation is included in the fully-discrete system of equations (70). For this purpose, it is assumed that the nodal values of the test functions take the admissible values $\mathbf{W}_{\mathbf{v}} = \mathbf{U}_{n+\frac{1}{2}}$ and $\mathbf{W}_{\mathbf{u}} = \mathbf{V}_{n+\frac{1}{2}}$. This yields

$$\mathbf{U}_{n+\frac{1}{2}} \cdot \hat{\mathbf{K}} \left(\mathbf{U}_{n+1} - \mathbf{U}_n \right) - \Delta t \, \mathbf{U}_{n+\frac{1}{2}} \cdot \tilde{\mathbf{K}}^{\mathrm{T}} \mathbf{V}_{n+\frac{1}{2}} = 0, \tag{75a}$$

$$\mathbf{V}_{n+\frac{1}{2}} \cdot \mathbf{M} \left(\mathbf{V}_{n+1} - \mathbf{V}_n \right) + \Delta t \, \mathbf{V}_{n+\frac{1}{2}} \cdot \tilde{\mathbf{K}} \mathbf{U}_{n+\frac{1}{2}} = \Delta t \, \mathbf{V}_{n+\frac{1}{2}} \cdot \mathbf{F}^{\mathrm{ext}} \left(t_{n+\frac{1}{2}} \right). \tag{75b}$$

It is possible to rewrite (75a) in the form

$$\Delta t \, \mathbf{V}_{n+\frac{1}{2}} \cdot \tilde{\mathbf{K}} \mathbf{U}_{n+\frac{1}{2}} = \left(\mathbf{U}_{n+1} - \mathbf{U}_n \right) \cdot \hat{\mathbf{K}} \mathbf{U}_{n+\frac{1}{2}}. \tag{76}$$

Inserting this relationship into (75b) and considering the symmetry of the mass matrix ultimately leads to (74). Consequently, the fully-discrete system of equations is indeed able to satisfy the discrete global energy balance in the sense that $E_{n+1} - E_n = \Delta t \mathbf{V}_{n+\frac{1}{2}} \cdot \mathbf{F}^{\mathrm{ext}}(t_{n+\frac{1}{2}})$.

3.3.3 | Notes on the Implementation

In the following, it is shown that the novel approach, like the conventional approach, can be implemented in an efficient manner. To this end, the fully-discrete system of equations (70) is reexpressed in a matrix-vector notation as

$$\begin{bmatrix} \mathbf{W}_{\mathrm{v}} \\ \mathbf{W}_{\mathrm{u}} \end{bmatrix} \cdot \begin{bmatrix} \mathbf{A}_{\mathrm{vu}} & \mathbf{A}_{\mathrm{vv}} \\ \mathbf{A}_{\mathrm{uu}} & \mathbf{A}_{\mathrm{uv}} \end{bmatrix} \begin{bmatrix} \mathbf{U}_{n+1} \\ \mathbf{V}_{n+1} \end{bmatrix} = \begin{bmatrix} \mathbf{W}_{\mathrm{v}} \\ \mathbf{W}_{\mathrm{u}} \end{bmatrix} \cdot \begin{bmatrix} \mathbf{f}_{\mathrm{v}} \\ \mathbf{f}_{\mathrm{u}} \end{bmatrix}, \tag{77}$$

where

$$\mathbf{A}_{\mathrm{vu}} = -\hat{\mathbf{K}}, \quad \mathbf{A}_{\mathrm{vv}} = \frac{1}{2}\Delta t\, \tilde{\mathbf{K}}^{\mathrm{T}}, \quad \mathbf{A}_{\mathrm{uu}} = \frac{1}{2}\Delta t\, \tilde{\mathbf{K}} = \mathbf{A}_{\mathrm{vv}}^{\mathrm{T}}, \quad \mathbf{A}_{\mathrm{uv}} = \mathbf{M}, \tag{78}$$

and

$$\mathbf{f}_{\mathrm{v}} = \mathbf{A}_{\mathrm{vu}}\mathbf{U}_n - \mathbf{A}_{\mathrm{vv}}\mathbf{V}_n, \quad \mathbf{f}_{\mathrm{u}} = \Delta t\, \mathbf{F}^{\mathrm{ext}}\left(t_{n+\frac{1}{2}}\right) - \mathbf{A}_{\mathrm{uu}}\mathbf{U}_n + \mathbf{A}_{\mathrm{uv}}\mathbf{V}_n. \tag{79}$$

Splitting the nodal displacement vector $\mathbf{U}_{n+1}$ and the nodal velocity vector $\mathbf{V}_{n+1}$ into a vector containing the unknown values $(\bullet)^{\mathrm{u}}_{n+1}$ and a vector containing the prescribed values at the Dirichlet boundaries $(\bullet)^{\mathrm{k}}_{n+1}$, respectively, allows (77) to be rewritten. In doing so, we assume that only boundary conditions on the displacement field can be prescribed, which imply corresponding boundary conditions on the velocity field. Taking these boundary conditions into account, the final system of linear equations can be stated as

$$\begin{bmatrix} \mathbf{A}^{\mathrm{uu}}_{\mathrm{vu}} & \mathbf{A}^{\mathrm{uu}}_{\mathrm{vv}} \\ \mathbf{A}^{\mathrm{uu}}_{\mathrm{uu}} & \mathbf{A}^{\mathrm{uu}}_{\mathrm{uv}} \end{bmatrix} \begin{bmatrix} \mathbf{U}^{\mathrm{u}}_{n+1} \\ \mathbf{V}^{\mathrm{u}}_{n+1} \end{bmatrix} = \begin{bmatrix} \bar{\mathbf{f}}_{\mathrm{v}} \\ \bar{\mathbf{f}}_{\mathrm{u}} \end{bmatrix}, \tag{80}$$

where for example, $\mathbf{A}^{\mathrm{uu}}_{\mathrm{vu}}$ refers to a submatrix of the matrix $\mathbf{A}_{\mathrm{vu}}$. Furthermore,

$$\bar{\mathbf{f}}_{\mathrm{v}} = \mathbf{f}^{\mathrm{u}}_{\mathrm{v}} - \mathbf{A}^{\mathrm{uk}}_{\mathrm{vu}}\mathbf{U}^{\mathrm{k}}_{n+1} - \mathbf{A}^{\mathrm{uk}}_{\mathrm{vv}}\mathbf{V}^{\mathrm{k}}_{n+1}, \quad \bar{\mathbf{f}}_{\mathrm{u}} = \mathbf{f}^{\mathrm{u}}_{\mathrm{u}} - \mathbf{A}^{\mathrm{uk}}_{\mathrm{uu}}\mathbf{U}^{\mathrm{k}}_{n+1} - \mathbf{A}^{\mathrm{uk}}_{\mathrm{uv}}\mathbf{V}^{\mathrm{k}}_{n+1}. \tag{81}$$

Similar to the conventional approach, the unknown nodal values can be determined successively. More precisely, applying the Schur complement allows the unknown nodal displacements to be determined from

$$\mathbf{A}_{\mathrm{eff}}\, \mathbf{U}^{\mathrm{u}}_{n+1} = \mathbf{f}_{\mathrm{eff}}, \tag{82}$$

where

$$\mathbf{A}_{\mathrm{eff}} = \mathbf{A}^{\mathrm{uu}}_{\mathrm{vu}} - \mathbf{A}^{\mathrm{uu}}_{\mathrm{vv}}(\mathbf{A}^{\mathrm{uu}}_{\mathrm{uv}})^{-1}\mathbf{A}^{\mathrm{uu}}_{\mathrm{uu}}, \quad \mathbf{f}_{\mathrm{eff}} = \bar{\mathbf{f}}_{\mathrm{v}} - \mathbf{A}^{\mathrm{uu}}_{\mathrm{vv}}(\mathbf{A}^{\mathrm{uu}}_{\mathrm{uv}})^{-1}\bar{\mathbf{f}}_{\mathrm{u}}. \tag{83}$$

The unknown nodal velocities then follow from

$$\mathbf{V}^{\mathrm{u}}_{n+1} = (\mathbf{A}^{\mathrm{uu}}_{\mathrm{uv}})^{-1}\left(\bar{\mathbf{f}}_{\mathrm{u}} - \mathbf{A}^{\mathrm{uu}}_{\mathrm{uu}}\mathbf{U}^{\mathrm{u}}_{n+1}\right). \tag{84}$$

Remark 3. Although the stiffness matrix $\tilde{\mathbf{K}}$ is unsymmetric, it can be inferred from (80) that the novel approach ultimately leads to a system of linear equations with a symmetric coefficient matrix. Likewise, $\mathbf{A}_{\mathrm{eff}}$ in the reduced system of linear equations (82) is symmetric.

Remark 4. Since the matrices (78) can be determined prior to the time-stepping loop for a given discretization, practical simulations with an efficient implementation of the formulation incur only minimal additional effort compared to standard formulations.

Remark 5. The implementation variant proposed above is valid only if $\mathbf{M}$ is invertible. However, in the elastostatic limit ($\rho = 0$), the unknown nodal displacements can be determined via

$$\mathbf{A}^{\mathrm{uu}}_{\mathrm{uu}}\, \mathbf{U}^{\mathrm{u}}_{n+1} = \mathbf{f}^{\mathrm{u}}_{\mathrm{u}} - \mathbf{A}^{\mathrm{uk}}_{\mathrm{uu}}\mathbf{U}^{\mathrm{k}}_{n+1}, \tag{85}$$

similar to the elastostatic case (see Section 2).

Remark 6. In this work, all occurring spatial integrals were evaluated numerically using Gaussian quadrature. Since all integrands arising in the novel approach are polynomial functions, exact numerical integration is, in principle, possible

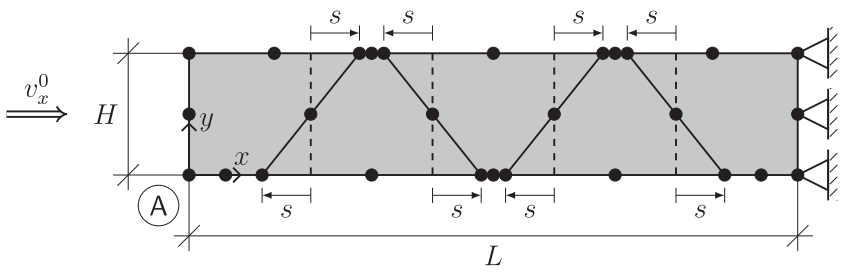

FIGURE 2 | Illustration of the spatially discretized bar-like structure.

(see [6] for a detailed discussion of numerical integration aspects in unsymmetric FE formulations). However, this would, in some cases, involve considerable computational effort. For instance, the exact evaluation of the contributions to $\hat{\mathbf{K}}$ would require the use of 6×6 integration points.

In the course of our numerical investigations, however, we found that the standard choice of 3×3 integration points appears to be sufficient for practical simulations. Further increasing the number of integration points had only a negligible effect on the results.

4 | Numerical Investigations

In this section, the different approaches for the dynamic extension dealt with in Section 3 are investigated using numerical examples.

Based on the designation of the underlying elastostatic formulation *UQ8**, summarized in Section 2, the individual elastodynamic formulations are denoted as *UQ8*-A1* for the formulation introduced in Section 3.1, *UQ8*-A2* for the one presented in Section 3.2, and *UQ8*-A3* for the one described in Section 3.3. As an additional benchmark formulation, denoted as *Q8*, the standard Bubnov-Galerkin serendipity element is employed, for which the implicit midpoint rule is used for the temporal discretization.

Unless stated otherwise, all simulations are carried out using the standard 3×3 Gaussian quadrature rule for the evaluation of the spatial integrals.

4.1 | Bar-Like Structure

In the first example, which also appears in [20], a bar-like structure subjected to an initial velocity is investigated. More precisely, a two-dimensional body (length $L = 5$, height $H = 1$) is considered, which is subjected to an initial velocity $v_x^0 = 10$ in the positive x-direction (cf. Figure 2). The problem is modeled in such a way that the initial velocity v_x^0 acts on every point of the body, except at the right boundary, where the velocity is set to zero due to the clamping.

The mass density of the body is assumed to be $\rho = 100$. Furthermore, Young's modulus is chosen as $E = 1 \times 10^6$, and Poisson's ratio is set to $\nu = 0$. Although the body is two-dimensional, the analytic solution for one-dimensional wave propagation can thus be employed. Consequently, the displacement field can be expressed as

$$u_x(\mathbf{x},\ t) = \sum_{n=1}^{\infty} A_n \sin(\omega_n t) \cos\Big((2n-1)\frac{\pi x}{2L}\Big), \quad u_y(\mathbf{x},\ t) = 0, \tag{86}$$

where

$$A_n = \frac{8 L v_x^0 (-1)^{n+1}}{((2n-1)\pi)^2 c}, \quad \omega_n = \frac{(2n-1)\pi c}{2L}, \quad c = \sqrt{\frac{E}{\rho}}, \tag{87}$$

while the velocity field follows as

$$v_x(\mathbf{x},\ t) = \sum_{n=1}^{\infty} A_n\ \omega_n \cos(\omega_n t) \cos\Big((2n-1)\frac{\pi x}{2L}\Big), \quad v_y(\mathbf{x},\ t) = 0. \tag{88}$$

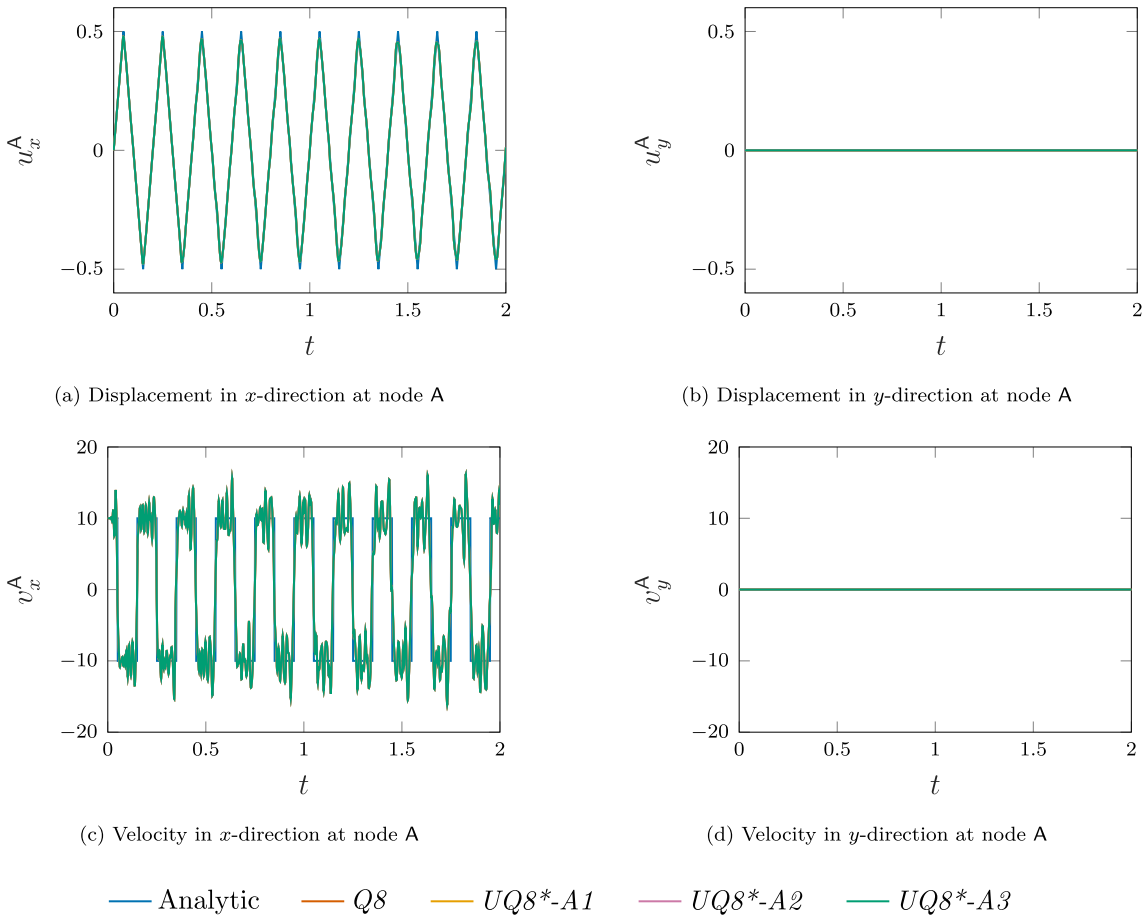

(a) Displacement in x-direction at node A

(b) Displacement in y-direction at node A

(c) Velocity in x-direction at node A

(d) Velocity in y-direction at node A

FIGURE 3 | Time evolution of the displacement field and the velocity field at a representative node of the bar-like structure obtained from simulations using a regular, undistorted mesh. With this mesh, all formulations yield identical results.

The purpose of this relatively simple problem is to illustrate the capabilities as well as the limitations of the different approaches for the dynamic extension. Two different meshes are used in the numerical investigations (see Figure 2): a regular, undistorted mesh ($s = 0$) and a distorted mesh ($s = 0.4$). All simulations are carried out with a prescribed total time $T = 2$ and a prescribed time step size $\Delta t = 0.001$.

4.1.1 | Simulation Results Obtained With a Regular, Undistorted Mesh

First, simulations are performed with a regular, undistorted mesh to show that, in this case, all formulations under investigation are equivalent[2] and yield sufficiently accurate results with the chosen finite element mesh and time step size. Specifically, the bar-like structure is spatially discretized with five square elements, each having a side length of 1.

During the simulations, the time evolution of the displacement field and the velocity field is recorded at the representative node A (coordinates: $(x,\ y) = (0,\ 0)$). The corresponding results are shown in Figure 3. Moreover, the time evolution of the total energy and the computed value of the parameter γ_n for a simulation using the *UQ8*-A2* formulation are presented in Figure 4. It can be observed that, for undistorted meshes, all formulations produce the same results and that the chosen discretization is sufficient to obtain reliable results.

4.1.2 | Simulation Results Obtained With *UQ8*-A1* and a Distorted Mesh

Next, it is demonstrated that the *UQ8*-A1* formulation should not be used with distorted meshes. To this end, a simulation is performed using the distorted mesh ($s = 0.4$), while all other simulation parameters remain unchanged. The corresponding results are given in Figure 5. It is clearly visible that simulations using this conventional approach are numerically unstable (see also [20] for similar results). Displacements increase without bound, and an energy blow-up

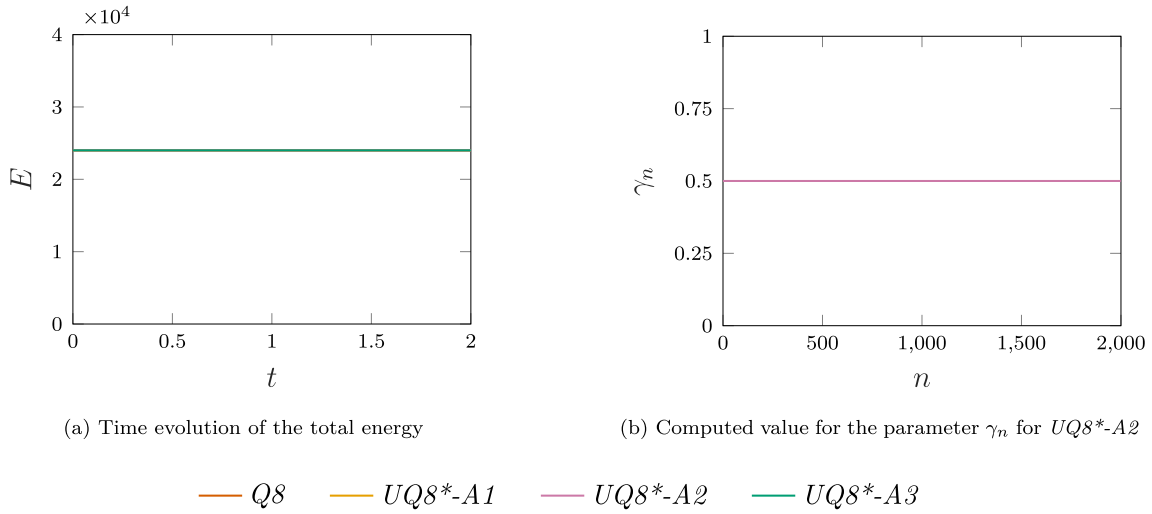

(a) Time evolution of the total energy

(b) Computed value for the parameter γ_n for *UQ8*-A2*

FIGURE 4 | Time evolution of the total energy and the parameter γ_n for the bar-like structure example obtained from simulations using a regular, undistorted mesh. With this mesh, all formulations yield identical results for the time evolution of the total energy.

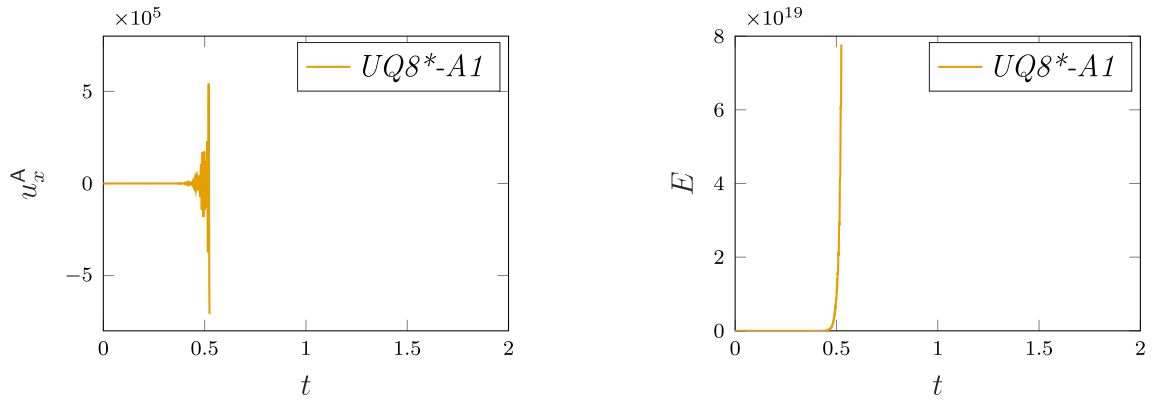

(a) Displacement in x-direction at node A

(b) Time evolution of the total energy

FIGURE 5 | Simulation results for the bar-like structure example obtained from a simulation using the *UQ8*-A1* formulation and a distorted mesh.

can be observed. After a few time steps, the simulation was terminated due to the occurrence of extremely large numerical values.

4.1.3 | Simulation Results Obtained With *UQ8*-A2* and a Distorted Mesh

The example was also simulated using the *UQ8*-A2* formulation and the distorted mesh ($s = 0.4$). It was found that this formulation is also only conditionally suitable for simulations involving distorted meshes.

As discussed in detail in Section 3.2, the formulation requires determining a value for the scalar parameter γ_n in every time step. This involves solving a quadratic equation. However, for the considered example, this equation ceases to have a real solution after a few time steps, making it impossible to determine a suitable value for γ_n and thus forcing the simulation to be terminated.

When using 3×3 integration points, this situation occurs at time step $n = 153$, whereas with 4×4 or more integration points, the simulation had to be terminated at time step $n = 1162$. Even when alternative strategies for determining γ_n – other than the one described in Section 3.2 – are applied, the simulation always had to be aborted after a limited number of time steps.

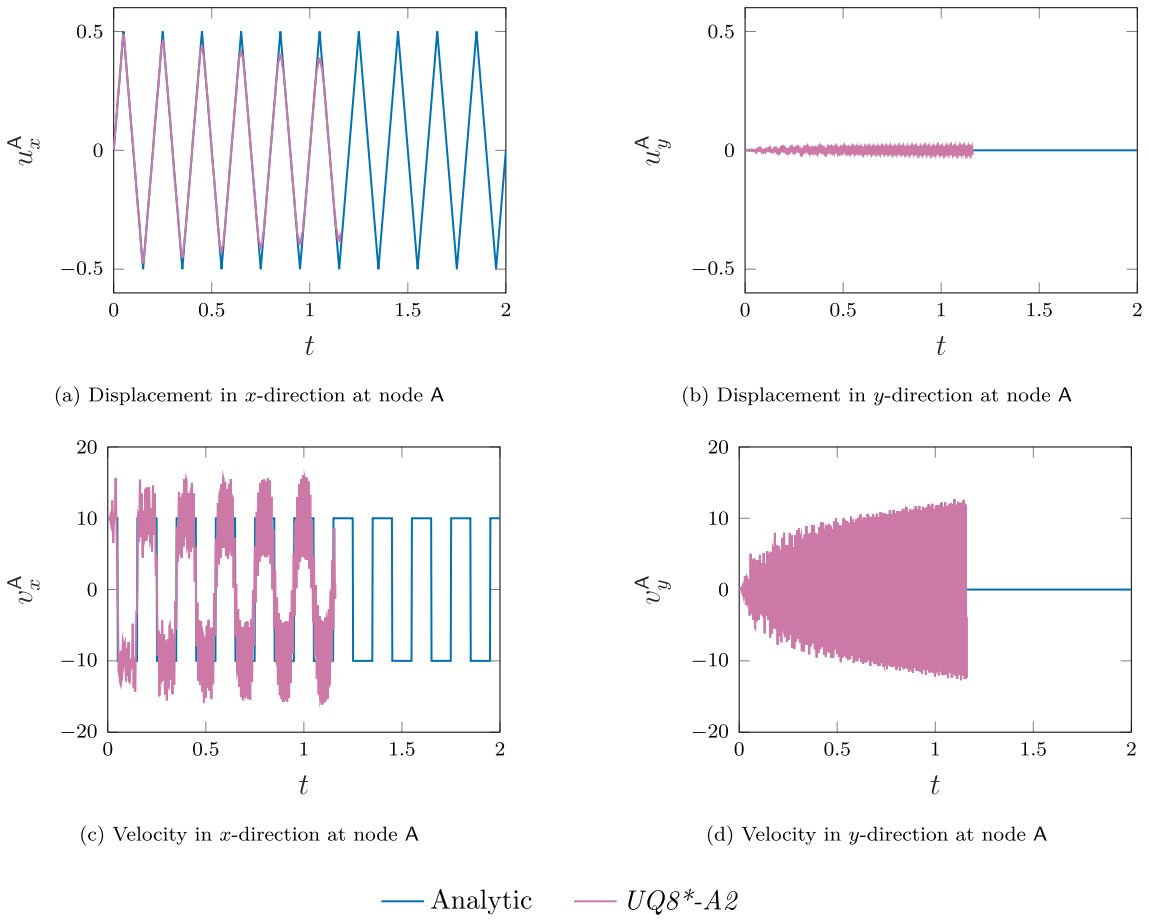

(a) Displacement in x-direction at node A

(b) Displacement in y-direction at node A

(c) Velocity in x-direction at node A

(d) Velocity in y-direction at node A

FIGURE 6 | Time evolution of the displacement field and the velocity field at a representative node of the bar-like structure obtained from simulations using the *UQ8*-A2* formulation and a distorted mesh.

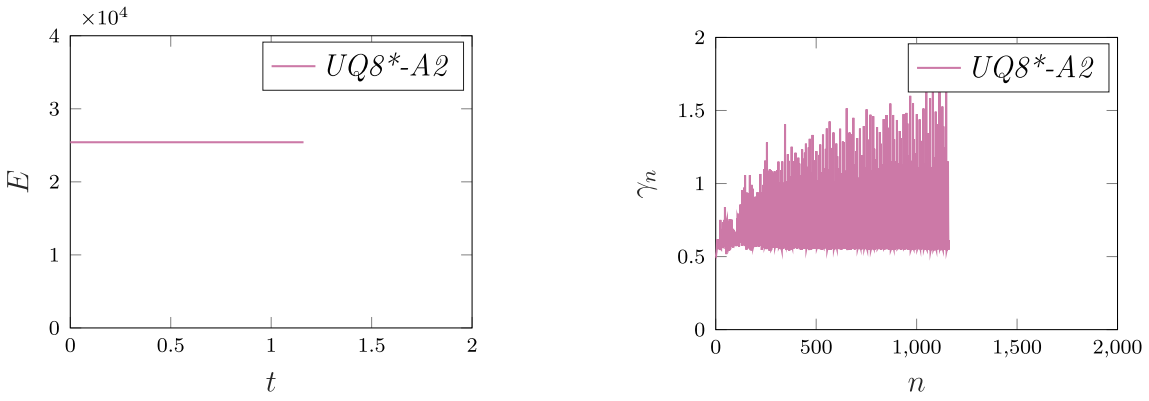

(a) Time evolution of the total energy

(b) Computed value for the parameter γ_n

FIGURE 7 | Time evolution of the total energy and the parameter γ_n for the bar-like structure example obtained from simulations using the *UQ8*-A2* formulation and a distorted mesh.

Figure 6 shows the time evolution of the displacement field and the velocity field at node A, computed using 4×4 integration points, up to the termination of the simulation. It is clearly visible that, as the simulation progresses, the computed results deviate increasingly from the analytic solution.

From Figure 7 it can be seen that the total energy remains constant, as required within the framework of the formulation, until the simulation is terminated. This figure also shows the computed value of the scalar parameter γ_n for each time step up to the termination of the simulation. It is evident that the value of this parameter varies significantly over the

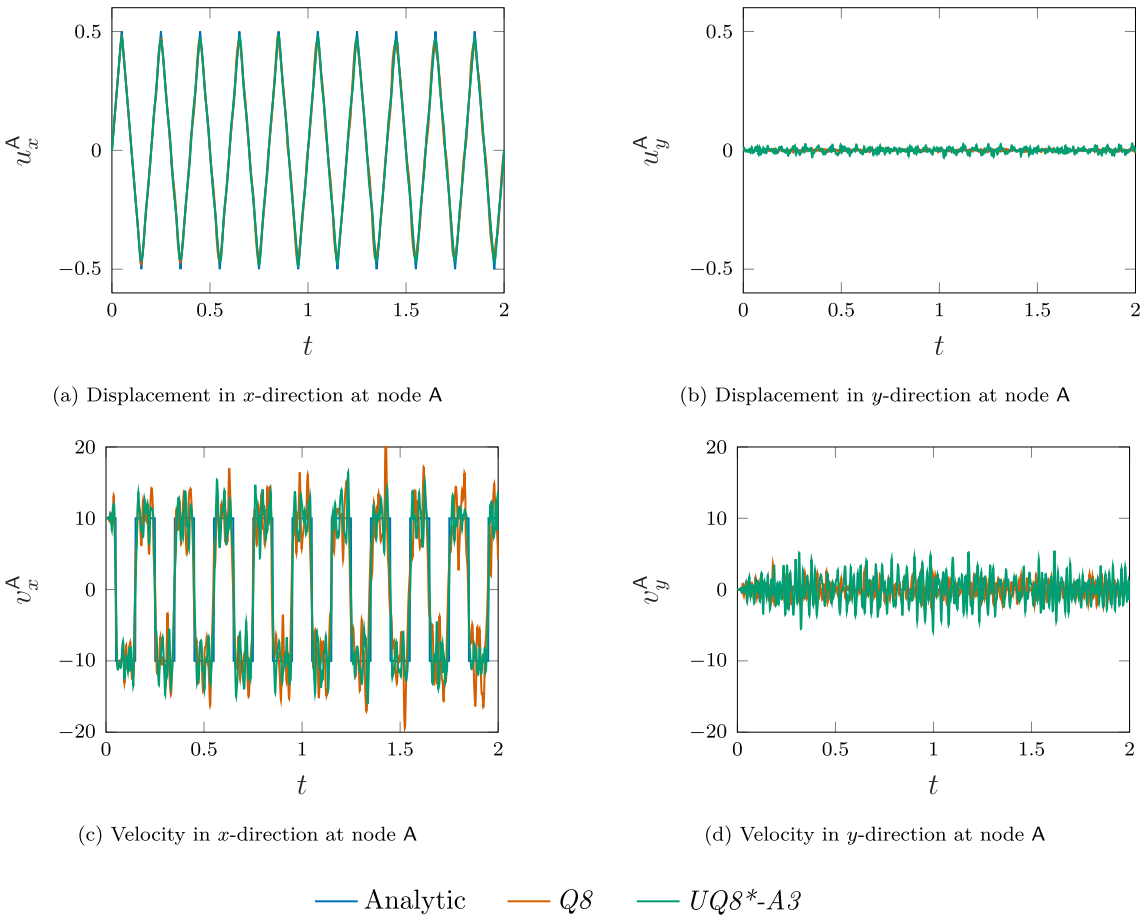

(a) Displacement in x-direction at node A

(b) Displacement in y-direction at node A

(c) Velocity in x-direction at node A

(d) Velocity in y-direction at node A

FIGURE 8 | Time evolution of the displacement field and the velocity field at a representative node of the bar-like structure obtained from simulations using the novel approach and a distorted mesh.

course of the simulation. In this process, the parameter also assumes values that are not allowed within the conventional Newmark method (cf. Remark 6).

4.1.4 | Simulation Results Obtained With *UQ8*-A3* and a Distorted Mesh

In the following, the results of simulations performed with the *UQ8*-A3* formulation and, for comparison, also with the *Q8* formulation are presented. Unlike the two formulations examined previously, these approaches remain stable even when the distorted mesh ($s = 0.4$) is used.

Figure 8 shows the time evolution of the displacement field and the velocity field at the representative node A. It can be seen that, for this example, both formulations yield similarly accurate results. Specifically, the computed displacements and velocities in the x-direction match the analytic solution about as well as those obtained in the simulations using the regular mesh (see Figure 3). However, the mesh distortion causes both formulations to predict nonzero displacements and velocities in the y-direction.

From Figure 9, it can be concluded that the *UQ8*-A3* formulation is indeed capable of correctly reproducing the constant time evolution of the total energy, even when a distorted mesh is used. The figure further demonstrates that the discrete global energy balance (71) is numerically satisfied for every time step.

4.2 | Beam-Like Structure

In the second numerical example, the novel *UQ8*-A3* formulation is shown to be less sensitive to mesh distortion than the standard *Q8* formulation. The comparison is carried out using the beam-like structure (length $L = 5$, height $H = 1$)

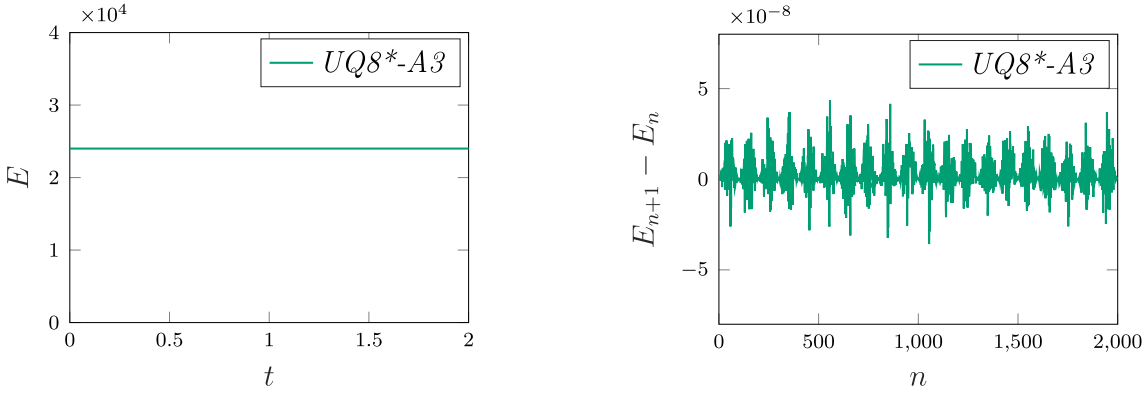

(a) Time evolution of the total energy

(b) Evaluation of the discrete global energy balance

FIGURE 9 | Energy results for the bar-like structure example obtained from a simulation using the *UQ8*-A3* formulation and a distorted mesh.

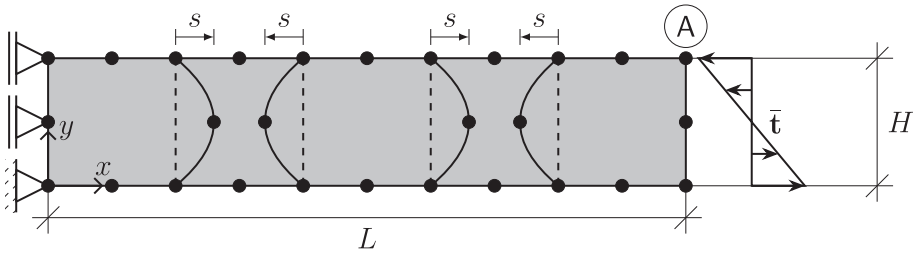

FIGURE 10 | Illustration of the spatially discretized beam-like structure.

shown in Figure 10. All simulations are performed under the assumption of a plane stress state, with a Young's modulus $E = 1 \times 10^7$ and a Poisson's ratio $\nu = 0.3$. As illustrated, the structure is supported at its left end.

In the following, the mesh sensitivity of the formulations is compared from different perspectives. In all cases, the structure is discretized using five finite elements. As illustrated, a regular mesh is obtained when the mesh distortion parameter is set to $s = 0$, whereas for $s \neq 0$ the elements become distorted. Since all other simulation parameters are kept constant, this setup enables a direct and isolated assessment of the influence of mesh distortion on the two formulations.

4.2.1 | Comparison Under Elastostatic Conditions

First, the two elastodynamic formulations are compared under elastostatic conditions. In this case, both formulations correspond to their respective elastostatic counterparts. It is already well established in the literature that the *UQ8** formulation (see Section 2) is generally less sensitive to mesh distortion than the standard 8-node Bubnov-Galerkin formulation. For the sake of completeness, these results are verified in the present work.

For this purpose, the resulting displacements due to a moment-type load applied at the right end of the structure are computed for both formulations. In particular, the traction forces are prescribed as $\bar{\mathbf{t}}(\mathbf{x},\ t) = f_{\max}\ f(t)\left(1 - \frac{2}{H}y\right)\mathbf{e}_x$, where $f_{\max} = 4 \times 10^5$ and $f(t) = t$. The total time is chosen as $T = 1$, and the problem is simulated using a single time step of size $\Delta t = T$. As the mass density is further set to $\rho = 0$, the resulting displacement field corresponds to the elastostatic solution of the problem, that is,

$$u_x(\mathbf{x}) = \frac{f_{\max}}{E}\left(x - \frac{2}{H}\,xy\right), \quad u_y(\mathbf{x}) = \frac{f_{\max}}{E}\left(-\nu\ y + \frac{1}{H}\,x^2 + \frac{\nu}{H}\,y^2\right). \tag{89}$$

If regular elements are used, this quadratic displacement field can be reproduced exactly by both formulations. However, when distorted elements are employed, only the *UQ8*-A3* formulation is still able to achieve this. The computed displacement values for the *Q8* formulation deviate increasingly from the exact solution as the elements become more severely distorted.

TABLE 1 | Displacement in y-direction at node A and its relative deviation from the exact solution for different values of the mesh distortion parameter s, computed using the *Q8* and the *UQ8*-A3* formulations for the beam-like structure example under elastostatic conditions.

		$s = 0$	$s = 0.1$	$s = 0.2$	$s = 0.3$	$s = 0.4$
Q8	u_y^{A}	1.0000	0.9502	0.8396	0.7199	0.6131
	rel. deviation	0.00%	4.98%	16.04%	28.01%	38.69%
UQ8-A3*	u_y^{A}	1.0000	1.0000	1.0000	1.0000	1.0000
	rel. deviation	0.00%	0.00%	0.00%	0.00%	0.00%

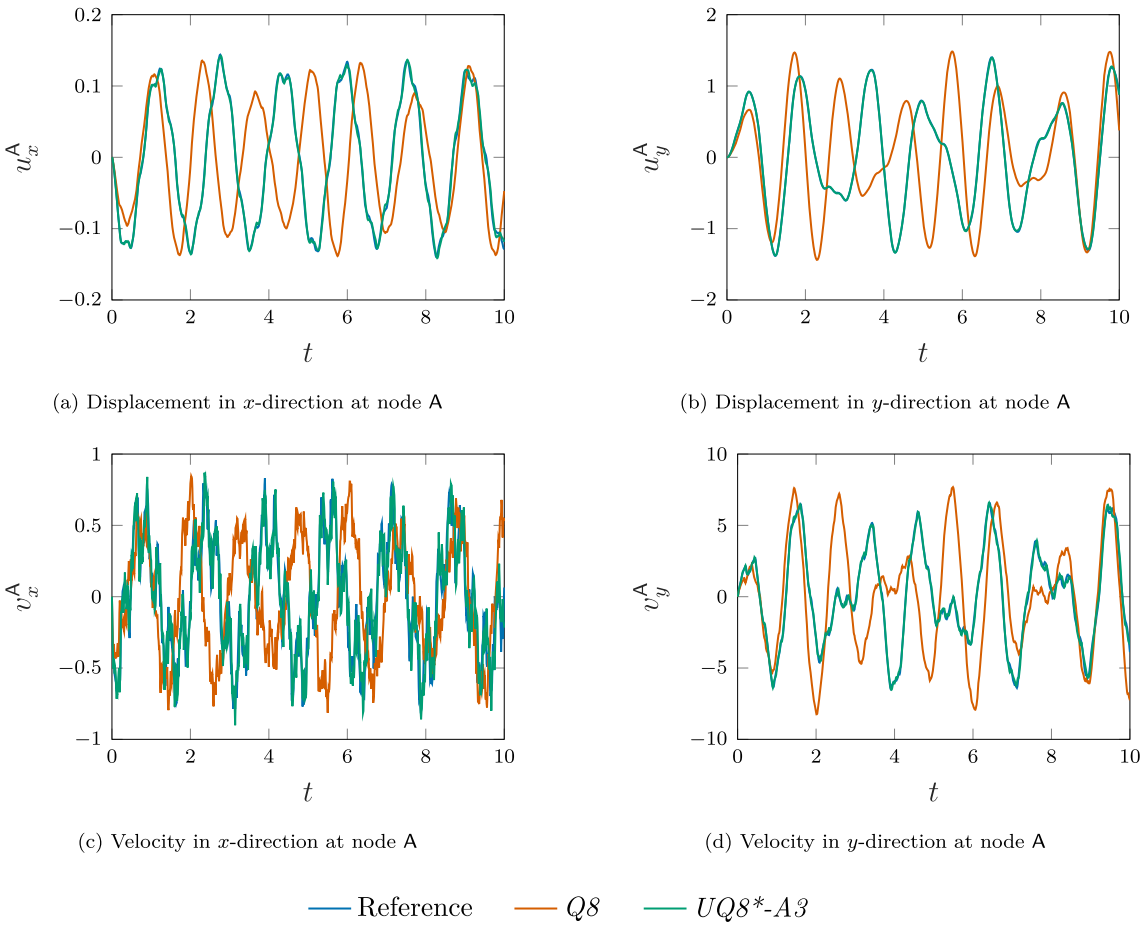

(a) Displacement in x-direction at node A

(b) Displacement in y-direction at node A

(c) Velocity in x-direction at node A

(d) Velocity in y-direction at node A

FIGURE 11 | Time evolution of the displacement field and the velocity field at a representative node of the beam-like structure obtained from simulations using the *Q8* and the *UQ8*-A3* formulation.

For clarification, Table 1 lists the computed displacement in y-direction at the representative node A (coordinates: $(x,\ y) = (L,\ H)$) and its relative deviation from the exact solution for different values of the mesh distortion parameter s. Under the given simulation parameters, the exact solution is $u_y^{\mathrm{A}} = 1$.

4.2.2 | Comparison Under Elastodynamic Conditions

Next, the mesh distortion sensitivity of the two formulations is assessed in the elastodynamic case through a comparison of the computed displacements and velocities. For this purpose, the mass density is set to $\rho = 1 \times 10^3$. The simulations are performed with a prescribed total time $T = 10$ and time step size $\Delta t = 0.01$. Furthermore, the traction forces are defined as $\bar{\mathbf{t}}(\mathbf{x},\ t) = f_{\max}\ f(t)\left(1 - \frac{2}{H}y\right)\ \mathbf{e}_x$, where $f_{\max} = 4 \times 10^5$ and $f(t) = \sin(2\pi t)$. Accordingly, in this case, the beam-like structure is subjected to a harmonic excitation.

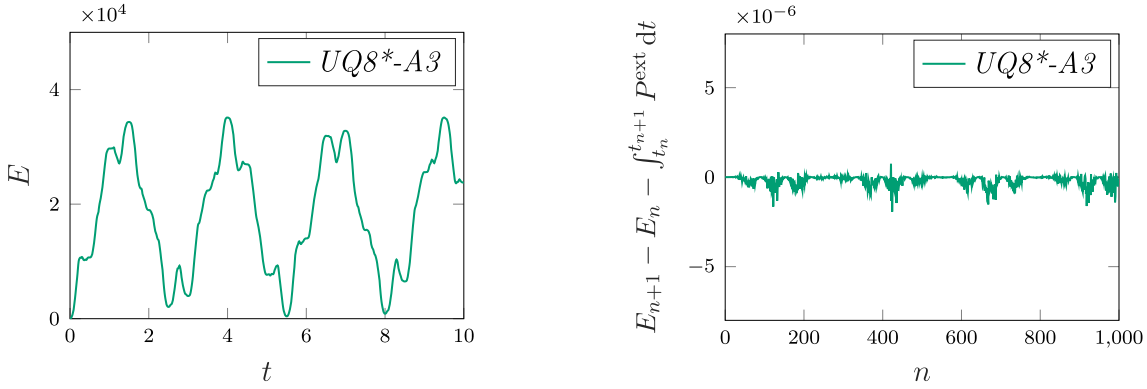

(a) Time evolution of the total energy

(b) Evaluation of the discrete global energy balance

FIGURE 12 | Energy results for the beam-like structure example obtained from a simulation using the *UQ8*-A3* formulation and a distorted mesh.

TABLE 2 | The first three natural frequencies of the beam-like structure obtained using the *Q8* formulation and the *UQ8*-A3* formulation for an undistorted mesh ($s = 0$) and a distorted mesh ($s = 0.4$).

		ω_1	ω_2	ω_3
Q8	$s = 0$	3.9611	21.2311	31.4016
	$s = 0.4$	4.6695	28.1110	31.5125
	rel. deviation	17.89%	32.40%	0.35%
UQ8-A3*	$s = 0$	3.9611	21.2311	31.4016
	$s = 0.4$	3.9604	21.1549	31.4021
	rel. deviation	0.02%	0.36%	0.00%

In a manner similar to the previous comparison, the time evolution of the displacement field and the velocity field is recorded at the representative node A (coordinates: $(x,\ y) = (L,\ H)$). First, simulations are performed using a regular mesh ($s = 0$) to obtain a reference solution. Subsequently, simulations are carried out using a distorted mesh ($s = 0.4$). The corresponding results are presented in Figure 11.

It can be observed that, similar to the findings of the elastostatic comparison, mesh distortion has a pronounced effect on the standard *Q8* formulation, whereas the *UQ8*-A3* formulation exhibits only minor deviations from the reference solution.[3] It therefore appears that the novel approach makes it possible to carry over the advantages of the underlying *UQ8** formulation with respect to mesh distortion sensitivity from elastostatics to elastodynamics.

Figure 12 shows, for a simulation using the *UQ8*-A3* formulation and the distorted mesh, the time evolution of the total energy as well as the evaluation of the discrete global energy balance (71) for every time step. The results demonstrate that this balance equation is also numerically satisfied when external loads act on the system.

4.2.3 | Comparison of Natural Frequency Approximations

In the final comparison, it is demonstrated that the novel *UQ8*-A3* formulation also appears to be significantly less sensitive to mesh distortion than the standard *Q8* formulation when approximating the natural frequencies of a structure. To this end, the first three natural frequencies of the beam-like structure are computed for both formulations using a regular ($s = 0$) and a distorted ($s = 0.4$) mesh. As in the previous comparison, the mass density is set to $\rho = 1 \times 10^3$.

Table 2 presents the results obtained with the different formulations. It can be observed that the sensitivity to mesh distortion of the *UQ8*-A3* formulation is smaller than that of the *Q8* formulation. The natural frequencies for the *Q8* formulation can be determined using standard procedures (see, e.g., [25]), whereas a suitable procedure for the *UQ8*-A3* formulation is outlined in Appendix B.

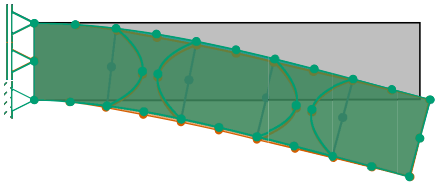

(a) Mode shapes associated with ω_1

(b) Mode shapes associated with ω_2

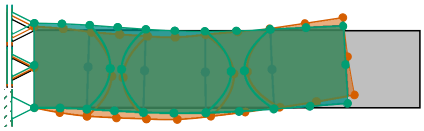

(c) Mode shapes associated with ω_3

Reference $(s = 0)$ — *Q8* $(s = 0.4)$ — *UQ8*-A3* $(s = 0.4)$

FIGURE 13 | Mode shapes of the beam-like structure obtained using the *Q8* formulation and the *UQ8*-A3* formulation for an undistorted mesh ($s = 0$) and a distorted mesh ($s = 0.4$).

Figure 13 additionally shows the first three mode shapes obtained with the different formulations and meshes. Here as well, the results indicate that the *UQ8*-A3* formulation is less sensitive to mesh distortions than the *Q8* formulation.

4.3 | Curved Beam-Like Structure

The objective of the final example is to demonstrate that the *UQ8*-A3* formulation inherits the order of accuracy of the implicit midpoint rule and thus corresponds to a second-order method. To this end, the curved beam-like structure shown in Figure 14 is considered, which is clamped at its right end.

The computations are carried out assuming an inner radius of $R_i = 9$ and an outer radius of $R_o = 11$. Furthermore, the mass density is prescribed as $\rho = 2000$. Additionally, a plane stress state is assumed, with Young's modulus $E = 2000$ and Poisson's ratio $\nu = 0.25$. At the left end of the beam, traction forces are applied in the form $\bar{\mathbf{t}} = -f(t)\ \mathbf{e}_y$, where the time-dependent load function is defined as

$$f(t) = \begin{cases} \sin\left(\frac{\pi}{5}t\right), & t \leq 5 \\ 0, & t > 5 \end{cases}. \tag{90}$$

The problem is simulated for a total time $T = 15$. As illustrated, the structure is spatially discretized using five finite elements. Although the elements in this example are already distorted due to the geometry of the structure, the mesh is intentionally distorted further to ensure a nonnegligible difference between the *UQ8*-A3* and the other formulations.

This can be confirmed by examining the time evolution of the total energy for the different formulations (see Figure 15). Once again, the simulation employing the *UQ8*-A1* formulation exhibits an energy blow-up. In the simulation with the *UQ8*-A2* formulation, no real value for the parameter γ_n can be determined after a few time steps. Only the simulation using the *UQ8*-A3* formulation yields satisfactory results. These results were obtained from simulations using a time step size of $\Delta t = 0.01$.

To determine the order of accuracy of the *UQ8*-A3* formulation, additional simulations are carried out with varying time step sizes Δt. After each simulation, the L_2 norm (see, e.g., [25]) is computed for both the error in the displacement field

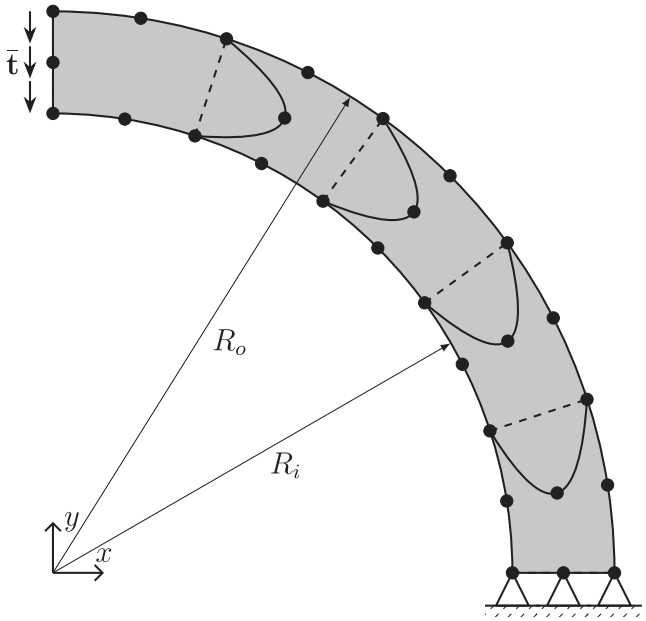

FIGURE 14 | Illustration of the spatially discretized curved beam-like structure.

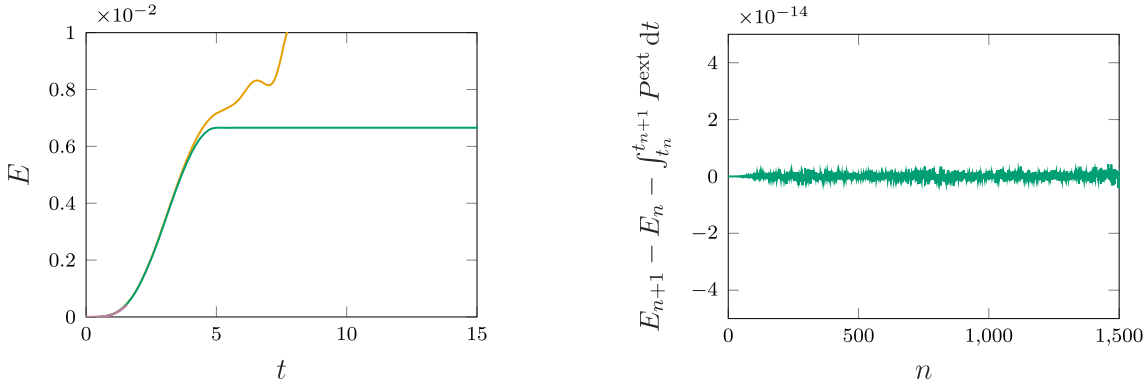

(a) Time evolution of the total energy

(b) Evaluation of the discrete global energy balance for the *UQ8*-A3* formulation

FIGURE 15 | Energy results for the curved beam-like structure example obtained from simulations using a time step size of $\Delta t = 0.01$.

$\mathbf{e_u}$ and the error in the velocity field $\mathbf{e_v}$ via

$$||\mathbf{e}_{(\bullet)}||_{L_2} = \left[\int_\Omega \left((\bullet)^{\text{ref}} - (\bullet)\right) \cdot \left((\bullet)^{\text{ref}} - (\bullet)\right) \mathrm{d}A\right]^{\frac{1}{2}}, \tag{91}$$

where the reference solution $(\bullet)^{\text{ref}}$ for the corresponding field is taken from a simulation with a time step size of $\Delta t = 1 \times 10^{14}$. As the results shown in Figure 16 indicate, the method is, as expected, second-order accurate (slopes of the regression lines are $(\mathbf{u},\ \mathbf{v}) = (2.0259,\ 2.0095)$).

5 | Conclusion

This contribution presents initial results on how mesh-distortion-insensitive Petrov-Galerkin FE formulations, originally developed for the linear elastostatic case, can be extended to linear elastodynamics. In this context, three

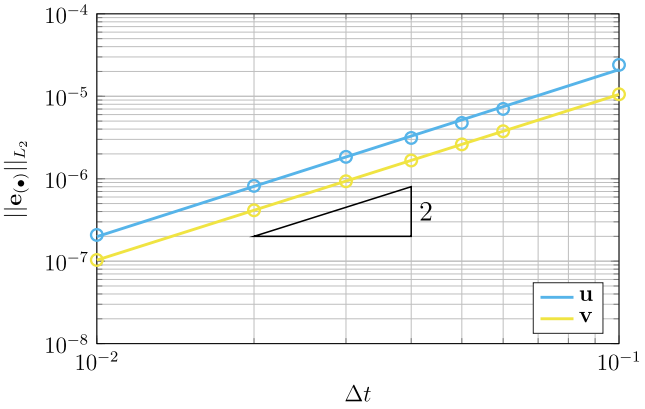

FIGURE 16 | Log-log plot showing the L_2 norm of the error in the displacement field and the error in the velocity field versus the time step size for the curved beam-like structure example.

different approaches are examined, building upon the established and relatively simple elastostatic formulation *UQ8** by Xie et al. [4].

The first approach reflects the standard procedure commonly used for Bubnov-Galerkin formulations. However, numerical investigations indicate that this approach is not suitable, as it is unstable and does not satisfy the global energy balance. As a consequence, nonphysical results are obtained, and simulations using this approach may even have to be terminated prematurely.

In the second approach, the procedure proposed in Wang and Hillman [20] is applied to the *UQ8** formulation. Numerical investigations indicate, however, that this strategy is likewise not suitable. Although the discrete global energy balance is satisfied by design, the numerical results demonstrate that substantial deviations from the analytic solution may develop over time. Furthermore, this approach may also lead to situations in which the simulation has to be terminated prematurely.

The proposed novel approach is the only method that provides satisfactory results within the numerical investigations. As shown in several examples, this approach enables the discrete global energy balance to be satisfied up to numerical round-off and allows stable simulations to be performed based on the *UQ8** formulation. Furthermore, the resulting formulation exhibits reduced sensitivity to mesh distortion compared to a standard 8-node Bubnov-Galerkin formulation. The mesh distortion insensitivity of unsymmetric finite element formulations, often observed for static problems, can thus be extended to the dynamic regime by applying the newly developed energy-consistent method.

Although the present investigations are limited to the *UQ8** formulation, it seems plausible that the insights gained may also be transferable to other mesh-distortion-insensitive Petrov-Galerkin FE formulations. Moreover, the extension of the proposed approach to nonlinear problems would be worth further investigation. Beyond the class of mesh-distortion-insensitive Petrov-Galerkin FE formulations, the present findings may also prove useful for the dynamic extension of other elastostatic formulations that lead to unsymmetric system matrices, such as isogeometric collocation methods (see, for example, [26] and the references therein).

Author Contributions

Felix Zähringer: conceptualization; formal analysis; investigation; methodology; project administration; software; validation; visualization; writing – original draft; writing – review and editing. **Peter Betsch:** conceptualization; methodology; formal analysis; supervision; resources; project administration; validation; funding acquisition; writing – original draft; writing – review and editing.

Acknowledgments

Open Access funding enabled and organized by Projekt DEAL.

Data Availability Statement

The computational code used to generate the results presented in this study is available from the corresponding author upon reasonable request.

Endnotes

[1]In a work by Kumar [19], the 20-node element introduced in [17] is employed to analyze the transient response of composite laminates to impacts. Temporal discretization is performed using Newmark's method. However, the conducted investigations therein are rather limited, and the issue of numerical instability has not been considered.

[2]The equivalence of the alternative schemes is due to the fact that the metric shape functions coincide with the serendipity shape functions in the case of regular element geometries (see Section 2).

[3]Similar to the previous example, a simulation using the *UQ8*-A1* or the *UQ8*-A2* formulation eventually exhibits numerical failure after a relatively small number of time steps.

[4]For simplicity, only fixed boundary conditions are considered here.

References

1. N.-S. Lee and K.-J. Bathe, "Effects of Element Distortions on the Performance of Isoparametric Elements," *International Journal for Numerical Methods in Engineering* 36, no. 20 (1993): 3553–3576, https://doi.org/10.1002/nme.1620362009.

2. S. Rajendran and K. M. Liew, "A Novel Unsymmetric 8-Node Plane Element Immune to Mesh Distortion Under a Quadratic Displacement Field," *International Journal for Numerical Methods in Engineering* 58, no. 11 (2003): 1713–1748, https://doi.org/10.1002/nme.836.

3. E. T. Ooi, S. Rajendran, and J. H. Yeo, "Remedies to Rotational Frame Dependence and Interpolation Failure of US-QUAD8 Element," *Communications in Numerical Methods in Engineering* 24, no. 11 (2008): 1203–1217, https://doi.org/10.1002/cnm.1026.

4. Q. Xie, K. Y. Sze, and Y. X. Zhou, "Modified and Trefftz Unsymmetric Finite Element Models," *International Journal of Mechanics and Materials in Design* 12 (2016): 53–70, https://doi.org/10.1007/s10999-014-9289-3.

5. K.-Y. Yuan, Y.-S. Huang, and T. H. H. Pian, "New Strategy for Assumed Stresses for 4-Node Hybrid Stress Membrane Element," *International Journal for Numerical Methods in Engineering* 36, no. 10 (1993): 1747–1763, https://doi.org/10.1002/nme.1620361009.

6. S. Eisenträger, E. Woschke, and E. T. Ooi, "Unsymmetric Serendipity Finite Elements: Performance Analysis," *Finite Elements in Analysis and Design* 254 (2026): 104487, https://doi.org/10.1016/j.finel.2025.104487.

7. S. Cen, G.-H. Zhou, and X.-R. Fu, "A Shape-Free 8-Node Plane Element Unsymmetric Analytical Trial Function Method," *International Journal for Numerical Methods in Engineering* 91, no. 2 (2012): 158–185, https://doi.org/10.1002/nme.4260.

8. Y.-F. Yang, Y.-Q. Huang, J.-Z. Wang, X.-C. Liu, and H.-B. Chen, "Two 8-Node Quadrilateral Unsymmetric Elements With Different Incompatible Modes Immune to Severe Distortion," *International Journal for Numerical Methods in Engineering* 124, no. 12 (2023): 2731–2755, https://doi.org/10.1002/nme.7226.

9. Y. Shang, S. Cen, and M.-J. Zhou, "8-Node Unsymmetric Distortion-Immune Element Based on Airy Stress Solutions for Plane Orthotropic Problems," *Acta Mechanica* 229 (2018): 5031–5049, https://doi.org/10.1007/s00707-018-2291-3.

10. Y. Shang and W. Ouyang, "4-Node Unsymmetric Quadrilateral Membrane Element With Drilling DOFs Insensitive to Severe Mesh-Distortion," *International Journal for Numerical Methods in Engineering* 113, no. 10 (2018): 1589–1606, https://doi.org/10.1002/nme.5711.

11. S. Cen, P.-L. Zhou, C.-F. Li, and C.-J. Wu, "An Unsymmetric 4-Node, 8-DOF Plane Membrane Element Perfectly Breaking Through MacNeal's Theorem," *International Journal for Numerical Methods in Engineering* 103, no. 7 (2015): 469–500, https://doi.org/10.1002/nme.4899.

12. L.-Z. Dou, Y.-Q. Huang, Y.-F. Yang, Y.-L. Ju, and H.-B. Chen, "A Novel Petrov-Galerkin 4-Node Quadrilateral Element With Radial Polynomial Interpolation for Linear Elastic Analysis," *International Journal for Numerical Methods in Engineering* 126, no. 10 (2025): e70049, https://doi.org/10.1002/nme.70049.

13. Y.-Q. Huang, Y.-F. Yang, J.-Z. Wang, X.-C. Liu, and H.-B. Chen, "Unsymmetric Extensions of Wilson's Incompatible Four-Node Quadrilateral and Eight-Node Hexahedral Elements," *International Journal for Numerical Methods in Engineering* 123, no. 1 (2022): 101–127, https://doi.org/10.1002/nme.6849.

14. Y. Huang, Y. Huan, and H. Chen, "An Incompatible and Unsymmetric Four-Node Quadrilateral Plane Element With High Numerical Performance," *International Journal for Numerical Methods in Engineering* 121, no. 15 (2020): 3382–3396, https://doi.org/10.1002/nme.6363.

15. R. Pfefferkorn and P. Betsch, "Mesh Distortion Insensitive and Locking-Free Petrov-Galerkin Low-Order EAS Elements for Linear Elasticity," *International Journal for Numerical Methods in Engineering* 122, no. 23 (2021): 6924–6954, https://doi.org/10.1002/nme.6817.

16. K. M. Liew, S. Rajendran, and J. Wang, "A Quadratic Plane Triangular Element Immune to Quadratic Mesh Distortions Under Quadratic Displacement Fields," *Computer Methods in Applied Mechanics and Engineering* 195, no. 9–12 (2006): 1207–1223, https://doi.org/10.1016/j.cma.2005.04.012.

17. E. T. Ooi, S. Rajendran, and J. H. Yeo, "A 20-Node Hexahedron Element With Enhanced Distortion Tolerance," *International Journal for Numerical Methods in Engineering* 60, no. 15 (2004): 2501–2530, https://doi.org/10.1002/nme.1056.

18. P.-L. Zhou, S. Cen, J.-B. Huang, C.-F. Li, and Q. Zhang, "An Unsymmetric 8-Node Hexahedral Element With High Distortion Tolerance," *International Journal for Numerical Methods in Engineering* 109, no. 8 (2017): 1130–1158, https://doi.org/10.1002/nme.5318.

19. S. Kumar, "Use of Unsymmetric Finite Element Method in Impact Analysis of Composite Laminates," *Finite Elements in Analysis and Design* 47, no. 4 (2011): 373–377, https://doi.org/10.1016/j.finel.2010.12.016.

20. J. Wang and M. C. Hillman, "Temporal Stability of Collocation, Petrov-Galerkin, and Other Non-Symmetric Methods in Elastodynamics and an Energy Conserving Time Integration," *Computer Methods in Applied Mechanics and Engineering* 393 (2022): 114738, https://doi.org/10.1016/j.cma.2022.114738.

21. N. M. Newmark, "A Method of Computation for Structural Dynamics," *Journal of the Engineering Mechanics Division* 85, no. 3 (1959): 67–94, https://doi.org/10.1061/JMCEA3.0000098.

22. S. Krenk, *Non-Linear Modeling and Analysis of Solids and Structures* (Cambridge University Press, 2009), https://doi.org/10.1017/CBO9780511812163.

23. M. Hille, P. Betsch, and M. Franke, "Port-Hamiltonian Formulation and Structure-Preserving Discretization of Finite Elasticity Based on a Mixed Hu-Washizu-Type Formulation," *Computer Methods in Applied Mechanics and Engineering* 458 (2026): 118790, https://doi.org/10.1016/j.cma.2026.118790.

24. V. Mehrmann and B. Unger, "Control of Port-Hamiltonian Differential-Algebraic Systems and Applications," *Acta Numerica* 32 (2023): 395–515, https://doi.org/10.1017/S0962492922000083.

25. O. C. Zienkiewicz, R. L. Taylor, and J. Z. Zhu, *The Finite Element Method: Its Basis and Fundamentals* (Butterworth-Heinemann, 2013), https://doi.org/10.1016/C2009-0-24909-9.

26. P. K. Masjedi, S. Jangravi, and A. Reali, "Isogeometric Collocation for Locking-Free Large Deflection Analysis of Geometrically Exact Beams With Intrinsic Formulation," *Computer Methods in Applied Mechanics and Engineering* 446 (2025): 118282, https://doi.org/10.1016/j.cma.2025.118282.

27. T. J. R. Hughes, *The Finite Element Method: Linear Static and Dynamic Finite Element Analysis* (Dover Publications, 2000).

Appendix A: Relationships Between Newmark's Method and Two Other Time Discretization Methods

In this part of the appendix, it is shown that certain relationships between Newmark's method and other time integration schemes, already known for Bubnov-Galerkin formulations, also hold for Petrov-Galerkin formulations.

First, the relationship between Newmark's method and the trapezoidal rule is addressed. For the parameter choice $\beta = \frac{1}{4}$ and $\gamma = \frac{1}{2}$, Newmark's method (39) corresponds to

$$\mathbf{U}_{n+1} = \mathbf{U}_n + \Delta t\, \mathbf{V}_n + \frac{1}{4}\Delta t^2 \left(\mathbf{A}_n + \mathbf{A}_{n+1}\right), \tag{A1a}$$

$$\mathbf{V}_{n+1} = \mathbf{V}_n + \frac{1}{2}\Delta t \left(\mathbf{A}_n + \mathbf{A}_{n+1}\right), \tag{A1b}$$

$$\tilde{\mathbf{M}}\mathbf{A}_{n+1} + \tilde{\mathbf{K}}\mathbf{U}_{n+1} = \mathbf{F}^{\text{ext}}_{n+1}. \tag{A1c}$$

Equation (A1a) can be rewritten as

$$\frac{1}{2}\left(\mathbf{A}_n + \mathbf{A}_{n+1}\right) = \mathbf{A}_{n+\frac{1}{2}} = \frac{2}{\Delta t^2}\left(\mathbf{U}_{n+1} - \mathbf{U}_n\right) - \frac{2}{\Delta t}\mathbf{V}_n. \tag{A2}$$

An admissible system state at time t_n satisfies

$$\tilde{\mathbf{M}}\mathbf{A}_n + \tilde{\mathbf{K}}\mathbf{U}_n = \mathbf{F}^{\text{ext}}_n. \tag{A3}$$

From $\frac{1}{2}$ ((A1c) + (A3)) it follows that

$$\tilde{\mathbf{M}}\mathbf{A}_{n+\frac{1}{2}} + \tilde{\mathbf{K}}\mathbf{U}_{n+\frac{1}{2}} = \mathbf{F}^{\text{ext}}_{n+\frac{1}{2}}. \tag{A4}$$

If relation (A2) is substituted into (A1b) and (A4), one obtains

$$\mathbf{V}_{n+1} = \frac{2}{\Delta t}\left(\mathbf{U}_{n+1} - \mathbf{U}_n\right) - \mathbf{V}_n, \tag{A5a}$$

$$\tilde{\mathbf{M}}\left(\frac{2}{\Delta t^2}\left(\mathbf{U}_{n+1}-\mathbf{U}_n\right)-\frac{2}{\Delta t}\mathbf{V}_n\right)+\tilde{\mathbf{K}}\mathbf{U}_{n+\frac{1}{2}}=\mathbf{F}^{\mathrm{ext}}_{n+\frac{1}{2}}, \tag{A5b}$$

which is identical to the time stepping method that can be obtained when evaluating (35) with the trapezoidal rule. This relationship, which is well known for Bubnov-Galerkin formulations (see, e.g., [27]), therefore also remains valid for Petrov-Galerkin formulations. A comparison of (A.5) with (37) and (38) further shows that Newmark's method, with the parameter choice $\beta=\frac{1}{4}$ and $\gamma=\frac{1}{2}$, is equivalent to the implicit midpoint rule in certain cases, for example, when the external forces are time-independent.

Appendix B: Determination of the Natural Frequencies When Using the Novel Approach

In this part of the appendix, it is outlined how the natural frequencies can be determined when using the novel approach. Starting from the semi-discrete Equation (64) and accounting for the boundary conditions,[4] the homogeneous equations of motion can be written in the form

$$\begin{bmatrix}\mathbf{A}^{\mathrm{uu}}_{\mathrm{vu}} & \mathbf{0}\\ \mathbf{0} & \mathbf{A}^{\mathrm{uu}}_{\mathrm{uv}}\end{bmatrix}\begin{bmatrix}\dot{\mathbf{U}}^{\mathrm{u}}\\ \dot{\mathbf{V}}^{\mathrm{u}}\end{bmatrix}+\begin{bmatrix}\mathbf{0} & \breve{\mathbf{A}}^{\mathrm{uu}}_{\mathrm{vv}}\\ \breve{\mathbf{A}}^{\mathrm{uu}}_{\mathrm{uu}} & \mathbf{0}\end{bmatrix}\begin{bmatrix}\mathbf{U}^{\mathrm{u}}\\ \mathbf{V}^{\mathrm{u}}\end{bmatrix}=\begin{bmatrix}\mathbf{0}\\ \mathbf{0}\end{bmatrix}, \tag{B1}$$

following the notation introduced in Section 3.3.3. Here, with slight deviations from the definitions given in (78),

$$\breve{\mathbf{A}}_{\mathrm{vv}}=\tilde{\mathbf{K}}^{\mathrm{T}},\quad \breve{\mathbf{A}}_{\mathrm{uu}}=\tilde{\mathbf{K}}=\breve{\mathbf{A}}^{\mathrm{T}}_{\mathrm{vv}}. \tag{B2}$$

These first-order differential equations can be transformed into the equivalent form

$$-\mathbf{A}^{\mathrm{uu}}_{\mathrm{vu}}\ddot{\mathbf{U}}^{\mathrm{u}}+\breve{\mathbf{A}}^{\mathrm{uu}}_{\mathrm{vv}}(\mathbf{A}^{\mathrm{uu}}_{\mathrm{uv}})^{-1}\breve{\mathbf{A}}^{\mathrm{uu}}_{\mathrm{uu}}\mathbf{U}^{\mathrm{u}}=\mathbf{0}. \tag{B3}$$

From this representation, the eigenvalues can be obtained by solving the corresponding generalized eigenvalue problem following standard procedures (see, e.g., [25]).